

Chapter 18

High Energy Emission from Pulsars and Pulsar Wind Nebulae

Kwong Sang Cheng

18.1 Introduction

Pulsars are accidentally discovered by the Cambridge scientists [48]. Shortly thereafter, Gold [39] and Pacini [72] proposed that pulsars are rotating neutron stars with surface magnetic fields of around 10^{12} G. Gold [39] pointed out that such objects could account for many of the observed features of pulsars, such as the remarkable stability of the pulsar period, and predicted a small increase in the period as the pulsar slowly lost rotational energy. With the discovery of the Vela pulsar with a period of 88 ms [65], the identification of the Crab pulsar with a period of 33 ms [86] and the discovery of slowdown of Crab pulsar [77], it was essentially confirmed that pulsars are rapidly rotating neutron stars. So far, over 1,500 radio pulsars have been found (see the most updated list of pulsars in www.atnf.csiro.au/research/pulsar/). The radio luminosities of these pulsars are small compared with the energy loss rate due to the pulsar spin down ($\sim 10^{-6}$ – 10^{-5}). Strong high-frequency radiation in the X-ray band has been observed from about two dozens pulsars (for recent review cf. [6, 7]), but only eight pulsars have been confirmed to emit high energy γ -rays (cf. [94] for a recent review). The observed radiated power for the γ -ray pulsars is concentrated mainly in the γ -ray range and the γ -ray luminosities are a substantial fraction (10^{-3} – 10^{-1}) of the spin-down power. This makes studies of high energy radiation from a pulsar a promising way to better understand the physical processes which result in their non-thermal radiation.

Theoretically, a common idea is that emissions ranging from radio to γ -rays are produced in different regions of the pulsar magnetosphere. To an excellent approximation, the pulsar may be considered as a non-aligned rotating magnet with a very strong surface magnetic field. Just outside the surface of the neutron star, the Lorentz force on a charged particle is very strong and far exceeds the force of gravitational

K.S. Cheng
Department of Physics, University of Hong Kong
e-mail: hrspksc@hkucc.hku.hk

attraction, i.e., $e((\mathbf{v}/c) \times \mathbf{B})/(GMm/r^2) \gg 1$. As a result, the structure of the magnetosphere of the neutron star is completely dominated by electromagnetic forces. Because the induced electric fields at the surface of a neutron star are so strong that the force on the charged particle in the surface exceeds the work function of the surface material, there must be a plasma surrounding the neutron star. In this way, there is a fully conducting plasma surrounding the neutron star, and electric currents can flow in the magnetosphere (e.g., [69]). If the component of the electric field $E_{\parallel} = \mathbf{E} \cdot \mathbf{B}/B$ along the magnetic field direction (\mathbf{B}) is non-zero in the pulsar magnetosphere, and this component of the electric field can accelerate particles to ultra-relativistic energies. The accelerated particles emit γ -rays due to curvature emission and other processes, e.g., inverse Compton scattering. Some of these γ -rays are absorbed giving rise to secondary electron-positron pairs. The created electron-positron pairs screen the electric field E_{\parallel} in the pulsar magnetosphere everywhere except for certain compact regions. The regions where E_{\parallel} is not screened are called accelerators or gaps. These gaps serve as an engine which is responsible for the pulsar non thermal radiation. There are two kinds of magnetosphere gaps: polar gaps and outer gaps, their location and potential drop being determined by the dipolar magnetic field, the rotation speed Ω and the angle between them called the inclination angle (α). The polar gaps place the source of the emission immediately above a magnetic pole. The evidence for the polar gaps came from radio observations of beam width and polarization. The outer gap place the source of emission far out in the magnetosphere, close to the velocity of light cylinder. The evidence for the origin of the outer gaps came from the high energy radiation observed from young pulsars such as the Crab, Vela and Geminga. It has been proved that all radiation from young pulsars cannot come from a single location.

We will organize this review paper as follows. In Sect. 18.2, we introduce the standard pulsar magnetosphere. In Sect. 18.3, we summarize some interesting observed X-ray and gamma-ray data. Some of these data look contradictory to each other. In Sect. 18.4, we review the high energy radiation produced by polar gaps and slot gaps. In Sect. 18.5, we introduce various outer magnetospheric gap models. In Sect. 18.6, we apply the three-dimensional outer gap to explain the observed phase-resolved spectrum and the polarization properties of the Crab pulsar. In Sect. 18.7, we introduce a simple pulsar wind nebula model, which can be used to explain high energy emission from region beyond the light cylinder. In Sect. 18.8, we use the simple pulsar wind model to explain the relation between the X-ray luminosity and the spin-down power. We also explain why millisecond pulsars in globular cluster behave so much different from those millisecond pulsars in the field. Finally we present a brief discussion in Sect. 18.9.

18.2 Standard Pulsar Magnetospheric Models

The standard emission theory for pulsars is based on the concept that pulsars are rapidly rotating, strongly magnetized, neutron stars. Detailed discussions of the structure of pulsar magnetospheres can be found, for example, in [69] and [9].

Here, we introduce some basic features of the magnetosphere of an aligned pulsar. It should be pointed out that these features do not differ drastically from those given by the more sophisticated treatments of oblique, self-consistent charged magnetospheres.

In an aligned pulsar, its magnetic dipole moment μ is aligned with its rotation axis Ω . The magnetic field far from the surface of the star is dominated by the dipole contribution of the star's intrinsic magnetic field. If the neutron star can provide the necessary negative charges (electrons) and positive charges (ions and/or positrons), and the currents in the magnetosphere are negligible, the electric field in steady state in the corotation frame, $\mathbf{E}' = 0$, which implies

$$\mathbf{E} + \frac{1}{c}(\Omega \times \mathbf{r}) \times \mathbf{B} = 0. \quad (18.1)$$

where \mathbf{E} and \mathbf{B} are the electric and magnetic fields measured in a non-rotating frame, and $\Omega \times \mathbf{r}$ is the co-rotating velocity. Equation (18.1) implies a local charge density

$$\rho_c = -\frac{\Omega \cdot \mathbf{B}}{2\pi c} \frac{1}{1 - |\Omega \times \mathbf{r}/c|^2}, \quad (18.2)$$

which is co-rotating with the local magnetic field. Such a charge density is called corotation charge density, or Goldreich–Julian charge density [40]. There are surfaces defined by $\Omega \cdot \mathbf{B} = 0$ on which this charge density is zero, called null charge surfaces. The charge density on both sides of the null charge surface are of different sign. This property plays an essential role in the formation of acceleration regions in the vicinity of null surfaces [15, 57]. Equation (18.2) corresponds to a charge number density $n_c = 7 \times 10^{-2} B_z P^{-1} (q/e)^{-1} \text{ cm}^{-3}$, where B_z is z -component of the magnetic field in gauss, P is the pulsar period in seconds and q/e is the charge of the particle in the charge unit of proton. The corotation region of the magnetosphere is limited to within a surface on which the magnetic field lines will be swept along at the speed of light. This cylindrical surface is called the light cylinder; it has a radius given by

$$R_L = c/\Omega \approx 5 \times 10^9 P \text{ cm}. \quad (18.3)$$

Field lines which cross the light cylinder do not return to the surface of the neutron star, and are referred to as open field lines. Otherwise, they are referred as closed field lines. The edge of the polar cap is defined by the locus of the last closed magnetic field lines (i.e., the field lines which just touch the light cylinder). In spherical polar coordinates, the radius of the polar cap region which contains the open field lines is given by $r_{pc} = R \sin \theta_{pc}$, where θ_{pc} is the angular radius of the polar cap. For an aligned pulsar with radius R (i.e., one with its rotation axis parallel to its magnetic axis), one can get

$$\sin \theta_{pc} = \left(\frac{R}{R_L} \right)^{1/2}, \quad (18.4)$$

since for dipole field lines $\sin^2 \theta / r = \text{constant}$ and the last closed field lines will touch the light cylinder at 90° . The polar cap radius is then given by

$$r_{pc} = R\theta_{pc} \approx 1.4 \times 10^4 R_6 P^{-1/2} \text{ cm}, \tag{18.5}$$

where R_6 is the stellar radius in units of 10^6 cm. Charged particles streaming out of the polar caps, which can escape to infinity along the open field lines, generate a toroidal magnetic field component. This toroidal component is largest near the critical field lines that separate the open from the closed regions. Because the potential at the base of the open field lines near the axis is negative with respect to the exterior, negative charges stream out. But, overall, a net charge cannot flow out from the star, so the potential of the magnetic field lines near the edge of the polar cap must be positive with respect to the exterior, and positive charges stream out from the star along these lines which form an annulus on the outer part of the polar cap. There is an intermediate set of critical field lines separating the regions of negative and positive outflow, and there the potential on the surface of the star equals the potential of the exterior interstellar medium. The magnetosphere of an aligned pulsar is shown in Fig. 18.1.

If, in addition, a strong potential is available to accelerate charge away from the stellar surface, a current of primary particles flows out from a single polar cap which is approximately given by

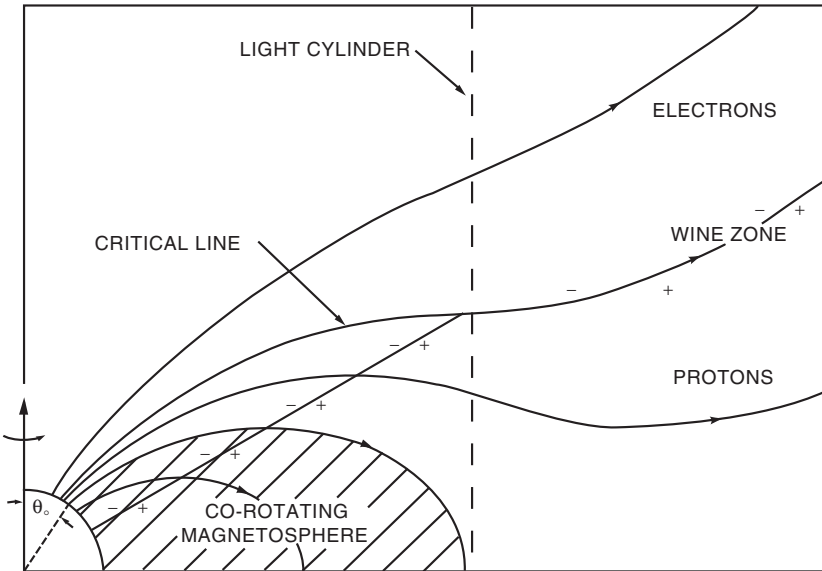


Fig. 18.1 Magnetosphere of an aligned pulsar. The *open-field lines* are swept back to form a toroidal component after crossing the light cylinder. The *closed-field lines* encompass the co-rotating portion of the magnetosphere. The *critical field line* divides regions of positive and negative current flow, while the *diagonal dashed line* gives the locus of $B_z = 0$ where the sign of the Goldreich–Julian space charge changes [40]

$$\dot{N}_{GJ} \approx \pi r_{pc}^2 \left(\frac{\rho_c}{e} \right) c \approx \frac{\Omega^2 R^3 B_s}{2ec} = 2.7 \times 10^{30} B_{12} P^{-2} R_6^3 \text{ s}^{-1}, \quad (18.6)$$

where B_s is the surface magnetic field. From (18.1) and (18.4), the potential difference between the center and the edge of the polar cap is

$$\Delta\Phi = \int \mathbf{E} \cdot d\mathbf{s} \approx \frac{\Omega^2 R^3 B_s}{2c^2} = 6.6 \times 10^{12} B_{12} P^{-2} R_6^3 \text{ V}. \quad (18.7)$$

The quantities given by (18.4), (18.6) and (18.7) define the characteristic polar cap values for the standard pulsar model.

Theoretically, it is suggested that high energy γ -rays from a pulsar are produced by the radiation of charged particles that are accelerated in the pulsar magnetosphere. Nowadays, two general types of γ -ray pulsar models are popular in the literature: polar cap models and outer gap models. Both models predict that electrons and positrons are accelerated in a charge depletion region, called a gap, by an electric field along the magnetic field lines and assume that charged particles lose their energies via some radiation mechanisms (say curvature radiation) in both polar and outer gaps. We introduce these models briefly in Sects. 18.4 and 18.5 respectively.

18.3 Summary of Some Interesting Observed Results in X-Rays and Gamma-Rays

In past two decades, there are tremendous progresses of X-ray and gamma-ray observations to rotation-power pulsars by ROSAT, ASCA, RXTE, BeppoSAX, CGRO, Chandra, XMM-Newton, INTEGRAL, etc. These satellites provide very important information for us to understand the properties of their emission regions including local energy distribution of charged particles, local electric field and magnetic field, geometry, etc. The observed information also constrains for theoretical models.

There are eight pulsars have been detected in gamma-ray energy range (cf. [94] for a recent review) with period ranging from 0.033 to 0.237 s and age younger than million years old. Most of these gamma-ray pulsars also emit X-rays (e.g., [6, 7]). However, there are over 50 pulsars detected with X-ray emission but most of them are old pulsars including more than 30 millisecond pulsars, which have age older than billion years.

Theoretically, it is suggested that high-energy photons are produced by the radiation of charged particles that are accelerated in the pulsar magnetosphere. There are two kinds of theoretical models: one is the polar gap model (e.g., [32, 43], for more detail review of polar cap model cf. [44]), and another is the outer gap model (e.g., [18, 19, 29, 33]). Both models predict that electrons and positrons are accelerated in a charge depletion region called a gap by the electric field along the magnetic field lines and assume that charged particles lose their energies via curvature

radiation in both polar and outer gaps. The key differences are: polar gaps are located near stellar surface and the outer gaps are located near the null charge surface, where are at least several tens stellar radii away the star.

The study of the emission characteristics from rotation powered pulsars has been a subject of long standing interest. Our knowledge of the fundamental properties (e.g., mass, spin, and magnetic field) of the underlying neutron star stems from detailed spectral and timing investigations. To facilitate an understanding of the mechanism by which the loss of rotational energy is converted into high energy radiation, many observational and theoretical studies have sought to determine the relationship between the X-ray luminosity, L_x , and the rate of rotational energy loss or spin down power, L_{sd} . Indeed, a correlation of the form $L_x \propto L_{sd}^{1.39}$ was found in Einstein data by [85]. Subsequent, [7, 8] used 27 rotation powered pulsars including 9 millisecond pulsars in the field and led to a relation of the form, $L_x \propto L_{sd}$ based on ROSAT data. However [84] used 16 rotation-power pulsars observed by ASCA and obtained a different relation, $L_x \propto L_{sd}^{1.5}$. Recently, a reanalysis of 39 pulsars based on data obtained from several X-ray satellites by [74] led to an intermediate relation $L_x \propto L_{sd}^{1.34}$, similar to that of [85]. However, the situation became more complicated when [42] reported that the MSPs in 47 Tuc obeyed a much shallower relation $L_x \propto L_{sd}^{0.5}$.

Qualitatively we believe that although the deduced existence of a correlation between L_x and L_{sd} suggests that the observed X-rays are produced by a process which taps the rotational energy of the neutron star, a detailed description of the mechanism remains elusive. This is, in part, a result of the fact that the data from different satellites are obtained in different energy ranges. The results can be affected, for example, by interstellar absorption especially for those pulsars studied in the soft X-ray regime of ROSAT (0.1–2.4 keV). In addition, the total X-ray luminosity is composed of contributions from both the pulsed and non pulsed components, and these components are likely to reflect physical conditions in diverse spatial environments. In general the pulsed thermal emission likely originates in regions within the light cylinder, where the magnetic field is so strong that radiation emission must be beamed. For examples, the pulsed non-thermal emission may be produced in the vicinity of the polar cap as a result of inverse Compton scattering of higher order generation pairs of particles on soft photons emitted by the neutron star [103] or in the outer magnetosphere as a result of synchrotron radiation of downward cascades from the outer gap electron/positron particles [26]. On the other hand, the non-thermal non pulsed X-ray radiation likely is produced in the surrounding wind nebula [27]. Since the pulsed and non pulsed emission have different origins, the relationship between the total X-ray luminosity and spin down power is not expected, in general, to be represented by a single power law. In fact, the non-thermal pulsed and non pulsed emission components are distinguished by different spectral signatures and conversion efficiencies.

The continuous observations of powerful young pulsars, including the Crab, the Vela and the Geminga, have collected large number of high energy photons, which allow us to carry out much more detailed analysis. Fierro et al. [36] divided the whole phase into eight phase intervals, i.e., leading wing, peak 1, trailing 1, bridge,

leading wing 2, peak 2, trailing 2 and off-pulse. They showed that the data in each of these phases can be roughly fitted with a simple power law. However, the photon indices of these phases are very different, they range from 1.6 to 2.6. Massaro et al. [68] have shown that X-ray pulse profile is energy dependent and the X-ray spectral index also depends on the phase of the rotation.

Recently [64] have combined the X-ray and gamma-ray data of the Crab pulsar, they showed that the phase-dependent spectra exhibit a double-peak structure, i.e., one very broad peak in soft gamma-rays and another broad peak in higher energy gamma-rays. The position of these peaks depend on the phase. Although the double-peak structure is a signature of synchrotron self-Compton mechanism, it is impossible to fit the phase dependent spectrum by a simple particle energy spectrum.

Actually it is not surprised that the spectrum is phase dependent because photons are emitted from different regions of the magnetosphere. The local properties, e.g., electric field, magnetic field, particles density and energy distribution are very much different for different regions. Therefore these phase dependent data provide very important information for emission region.

18.4 Polar Cap and Slot Gap Models

Sturrock [89] first proposed the polar cap model, and later many authors (e.g., [2, 4, 31, 43, 83]) developed it. Sturrock [89] studied the consequences of the particle outflow from the star along the open field lines. Assuming that the electric field is primarily radial for heights $h < r_{pc}$ and transverse at heights $h > r_{pc}$, primary charged particles (e.g., e^\pm pairs) are accelerated in a small zone with typical height h above the polar cap surface, and the primary emission region is confined to the dipole open field lines. Using the approximation $\rho_c = (1/4\pi)\nabla^2\Phi \sim (1/4\pi)\Phi/h^2$ and (18.2), the accelerating potential responsible for the charged particle flow given by (18.6) is $\Phi \sim (2\Omega B_s/c)h^2$. The potential difference between the center and the edge of the polar cap is

$$\Delta\Phi \sim (\Omega B_s/2c)h^2. \quad (18.8)$$

Sturrock assumed that $h \sim r_{pc}$, so $\Delta\Phi \sim (\Omega^2 R^3 B_s/2c^2)$, which is essentially equivalent to (18.7), and amounts to a potential drop of $\Delta V \sim 6 \times 10^{12} B_{12} P^{-2} R_6^3$ V. Sturrock further assumed that this potential would be sufficient to rip charged particles (say electrons) from the stellar surface and accelerate them up to relativistic velocities along the strong magnetic field lines. The perpendicular energies of the accelerated electrons would be rapidly radiated away through synchrotron radiation, but their longitudinal energies would be radiated away in form of high energy γ -rays due to curvature radiation mechanism, which is the dominant energy lost process for charged particles moving with relativistic velocity along the curved magnetic field lines. The typical curvature photon energy is

$$E_\gamma \approx (3/2)\hbar\gamma_e^3/s \sim 10^9 \gamma_7^3 s_8^{-1} \text{ eV}, \quad (18.9)$$

where γ_7 is the electron Lorentz factor in units of 10^7 , and $s_8 \sim (rR_L)^{1/2}/10^8$ is the typical curvature radius in units of 10^8 cm. When these extremely energetic photons move transverse to the strong magnetic field, they will produce e^\pm pairs via $\gamma + B \longrightarrow e^+e^-$. Sturrock therefore envisaged that, for a sufficiently strong electric field, these secondary pairs would also be accelerated and create γ -rays leading to further pairs, resulting in a pair cascade. This cascade produces the coherent low frequency emission necessary to explain the brightness temperature implied from radio observations. From (18.7), as the pulsar slows down, the potential drop will decrease, and would eventually reach the critical value below which pair production will not be possible and pulsed emission will cease. However, (18.8) means that the acceleration of charged particles is caused by the full vacuum potential across the polar cap, which is now recognized to be incorrect. In fact, the charged particles will only be accelerated in the vacuum gap where $\mathbf{E} \cdot \mathbf{B} \neq 0$ (see below).

Ruderman and Sutherland [83] carried out a major development of this model, and addressed some of the concerns associated with the standard pulsar model, such as trying to maintain a force-free $\mathbf{E} \cdot \mathbf{B} = 0$ condition while the charge density moves everywhere at the speed of light along divergent field lines. In their model $\Omega \cdot \mathbf{B} < 0$, therefore the polar cap electric field can only pull out ions. Since electrons will not be stripped from the stellar surface while the ions will be retained due to their higher surface binding energy, the stellar surface does not supply the positive charges to replace the positive charges in the magnetosphere which are accelerated outward, as a result a vacuum gap will form above the polar cap. This gap will continue to expand at a speed $\sim c$ until it reaches a maximum height h , which corresponds to a gap potential large enough to ignite an e^\pm cascade. In the vacuum gap, $\mathbf{E} \cdot \mathbf{B} \neq 0$, it means that the magnetic field lines in this region are not forced to co-rotate. Above the vacuum gap, the magnetosphere co-rotates with the pulsar. The gap potential and h can be determined by the condition of pair production which is

$$\frac{E_\gamma}{2m_e c^2} \frac{Bh/s}{B_q} \geq \frac{1}{15} \quad (18.10)$$

[35, 83]. Since the electrons/positrons are accelerated in the gap, $\gamma_e = e\Delta\Phi/m_e c^2$. Combining (18.8)–(18.10), we obtain

$$h_{RS} = 5 \times 10^3 s_6^{2/7} P^{3/7} B_{12}^{-4/7} \text{ cm} \quad (18.11)$$

and

$$\Delta\Phi \equiv \Delta V_{RS} = 1.6 \times 10^{12} s_6^{4/7} P^{-1/7} B_{12}^{-1/7} \text{ V}. \quad (18.12)$$

Here s_6 is the radius of curvature in units of 10^6 cm instead of 10^8 cm, it is because non-dipolar field with a characteristic curvature radius $\sim 10^6$ cm is assumed to exist on the neutron star surface. Ruderman and Sutherland suggested that, when the gap potential drop reaches ΔV_{RS} , a spark discharge occurs inside the gap, triggering an avalanche of e^\pm pairs, which in turn will result in the pair production cascade envisaged by Sturrock. The difference from Sturrock's model is that here the acceleration occurs only in the vacuum gap ($\mathbf{E} \cdot \mathbf{B} \neq 0$) with height $h = h_{RS} < r_{pc}$. Outside the gap

($\mathbf{E} \cdot \mathbf{B} = 0$), the pairs are no longer accelerated and stream outward with a Lorentz factor ~ 3 . Ruderman and Sutherland showed that the density of the streaming pairs is much higher than the Goldreich–Julian density, so the plasma will be essentially charge neutral. Furthermore, they suggested that radio emission occurs above the spark regions in the filled, streaming region where bunching by plasma instabilities would lead to coherent radio emission.

When $\Omega \cdot \mu > 0$, the polar cap charge density is negative. Electrons with much weaker binding energy can be pulled out from the stellar surface and form a steady outflow current. Because of the finite inertia of the electron, the potential of the polar gap cannot be zero. Arons and Scharlemann [4] presented solutions for steady, space charge limited flow (which is shorted out by pair creation) of an electron beam above the polar cap of a pulsar in this case. Because of curvature of the magnetic field, the space charge limited particle beam from the stellar surface is accelerated to an energy high enough to emit curvature γ -rays. The particles accelerate along the magnetic field through a potential drop [4]

$$\Delta V_s \approx \frac{\Omega^2 \mu R}{c^2} \frac{R}{s} \sim 10^{11} \mu_{30} P^{-5/2} \text{ V}, \quad (18.13)$$

which is called the space-charge-limited potential (also see [3] for a review). However, [71] have shown that the actual potential drop for the space-charge-limited flow is much larger than that in (18.13) if the inertial frame dragging effect is included. The corrected space-charge-limited potential should be

$$\Delta V_s \approx \frac{10R}{s} \frac{\Omega^2 \mu}{c^2} [1 - (R/r)^3] \sim 10^{14} \mu_{30} P^{-5/2} [1 - (R/r)^3] \text{ V}, \quad (18.14)$$

which is even larger than ΔV_{RS} , where μ_{30} is the pulsar's magnetic moment in units of 10^{30} cgs and s is the radius of curvature of the magnetic field lines. It is further suggested that a large potential drop may explain γ -ray emission from young pulsars (e.g., [70]). However, (18.14) has ignored the pair production inside the gap which is possible if the surface magnetic field is pure dipolar, otherwise the pair cascade should restrict the potential of the cap as shown in (18.12). Harding and Muslimov [45] have investigated a self-consistent particle acceleration mechanism by the electrostatic field due to the effect of inertial dragging near the polar cap. They computed the potential self-consistently, including pair formation in the polar gap.

In explaining the high energy emission from pulsars, [32] have used the traditional polar cap model to calculate the light curve and gamma-ray spectrum. They provided a very successful model fitting for the observed phase average spectrum of the Vela pulsar. However, they have to artificially put the acceleration region at three stellar radii and assume the polar cap rim enhancement. The viewing angle is assumed to be 10° . All these assumptions are not easy to be justified.

In order to seeking the possibility of a wide hollow cone emission due to flaring B -field lines, [2] first examined a gap formation in higher altitudes along the last open field line. This type of accelerator is called slot gap. The more recent review of slot gap can be found in [44]. Based on the slot gap properties, some light curve and

polarization properties of the Crab pulsar can be explained very well (cf. [33, 34]). Another successful application of slot gap is in millisecond pulsars, [46] have used the slot gap geometry and assumed that secondary particles can maintain their pitch angles due to the interaction with the radio. The model predictions can explain the observed high energy radiation spectrum of the millisecond pulsar PSR J0218+4232 very successfully.

18.5 Outer Gap Models

18.5.1 CHR Model

Cheng et al. [18, 19], (hereafter CHRI and CHR II) constructed a semi-analytical outer-magnetospheric gap model of rapidly spinning neutron stars. They assumed that a global current flow pattern through the magnetosphere of a rapidly spinning magnetized neutron star results in large regions of magnetospheric charge depletion (gaps). This would result in a large electric field along the magnetic field lines ($\mathbf{E} \cdot \mathbf{B} \neq 0$) in those regions, which, through various mechanisms, including inverse Compton scattering and photon-photon pair production, could sustain enough e^\pm pair production to:

1. Short out $\mathbf{E} \cdot \hat{\mathbf{B}}$ except in an almost slab like volume (the “outer gap”)
2. Maintain the huge magnetospheric current flow

According to this model, there are two kinds of pulsars: Crab-type and Vela-type pulsars. For the Crab-type pulsars, a Crab-type gap produces GeV photons via curvature radiation and subsequently produce e^\pm which radiate synchrotron radiation and inverse Compton-scattered photons (CHRII; [24, 56]). The detailed pair production and radiation mechanisms of the Vela-type outer gap (for the conditions in pulsars with a Vela-type outer gap refer to CHRII; [16]) are the following. The members of paired e^\pm are created within the gap (primary pairs) and accelerated in opposite direction to extreme relativistic energies. These primary e^\pm produce γ -rays (primary) through inverse Compton scattering on IR photons. Here primary γ -ray are sufficiently energetic to produce e^\pm pairs (secondary) in collision with the same IR photon flux; synchrotron radiation of these secondary pairs gives crossed fan beams of secondary γ -rays and weaker ones of X-rays. Collisions of the secondary γ -rays and X-rays produce a large flux of lower energy e^\pm pairs (tertiary), much further from the outer gap, which fill much of the outer-magnetosphere. It is the (tertiary) IR synchrotron radiation from tertiary pairs through the outer gap which causes the initial primary inverse Compton scattering in the gap and converts the scattered γ -rays, thus initiating the entire series of pair production processes. It should be noted that in Vela-like pulsars the CHR model use the infrared photons to extract energy from the outer gap via Inverse Compton Scattering with the primary particles which predicts a large observed TeV flux, which has not yet been observed

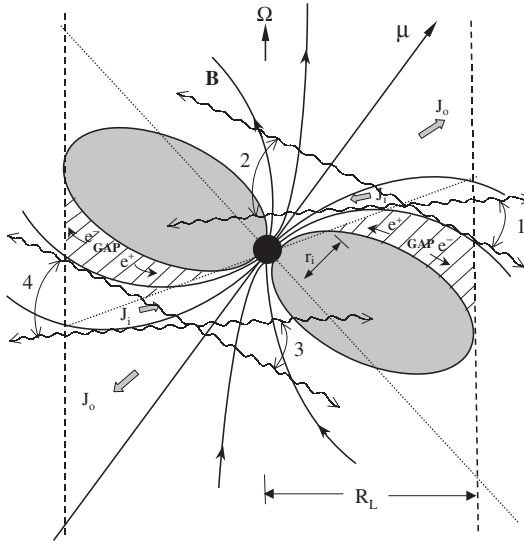


Fig. 18.2 Schematic illustration of the location and geometry of the outer gaps, the current flow pattern in the magnetosphere and the radiation beaming of secondary radiation from four emission regions. The outer gaps, where $E \cdot \hat{B} \neq 0$, starts at r_i where the null surface intersect the last closed field lines and extends to R_L

(e.g., [96]). Figure 18.2 schematically shows the location of the outer gap and the radiation beaming of secondary radiation from the two emission regions.

The pair production and radiation mechanisms of the Vela-type outer gap and the Crab-type outer gap are quite different. The primary e^\pm of the Crab pulsar lose most of their energies via curvature radiation instead of synchrotron radiation as in the case of the Vela pulsar. As a result, the power of the Crab-type and Vela-type pulsars have different parametric dependence on P and B_s . The radiation power loss of the Crab-type pulsars is given by

$$L_\gamma \simeq 1.5 \times 10^{37} P \text{ erg s}^{-1}. \tag{18.15}$$

On the other hand the radiation power loss of the Vela-type is very sensitive to the spin period P as well as the dipole magnetic field strength B and it is given by $L_\gamma \propto P^{-4} B_s^2$.

In calculating the γ -ray spectrum of the Vela pulsar, Cheng Ho and Ruderman (CHRI, II) made some simplifying assumptions. They argue that the secondary e^-/e^+ production distribution in the Vela-type outer gap would scale like γ^{-1} , where γ is the e^-/e^+ Lorentz factor and most of the secondary e^\pm have similar pitch angles, θ , with respect to the local magnetic field, B . Then the steady state distribution is roughly given by [12],

$$N_e(\gamma) \sim \gamma^{-2} \ln \left(\frac{\gamma_{max}}{\gamma} \right), \tag{18.16}$$

where γ_{max} is the maximum energy of the primary e^-/e^+ which is determined by the fact that the energy of the primary photons must be just enough to make pairs on collision with the IR photons with a typical energy, E_{IR} , therefore, $\gamma_{max} \sim mc^2/E_{IR}$. The typical energy of the IR photons is estimated to be (CHRII)

$$E_{IR} \sim \frac{\hbar}{\omega_B^3} \left(\frac{mc^3 \Omega}{e^2} \right)^2, \quad (18.17)$$

where $\omega_B = \frac{eB}{mc}$, $B(r) = B_s R^3/r^3$ for a dipole field, $r \equiv \eta R_L$ is the observed emission distance to the outer gap and R is the stellar radius. Because the maximum energy of secondary e^\pm is $\gamma_{max} mc^2$, the typical energy of the synchrotron photons from the secondary e^\pm is [16]

$$E_{max} = 9 \times 10^5 \eta^{-21} P_{-1}^{17} B_{12}^7 \sin \theta \text{ eV}, \quad (18.18)$$

where θ is the mean pitch angle of the secondary pairs with respect to the local magnetic field and αR_L is the mean distance to the outer gap. If the primary photons are emitted tangential to the local field then $\sin \theta \approx (\frac{1}{\gamma_{max}} + \frac{\lambda}{S}) \sim \lambda/S$ where λ is the mean free path of the primary photons and S is the radius of curvature of the local magnetic field lines. In general, $\sin \theta$ should vary from pulsar to pulsar. For $E_\gamma > E_{max}$, the photon flux will drop exponentially, so this energy is regarded as an upper spectral cut-off. Because of the weakness of the magnetic field in the outer magnetosphere of Vela-type pulsars, a relativistic e^-/e^+ does not radiate away all of its energy through synchrotron loss before it leaves the light cylinder. Thus, the distribution of secondary pairs given by (18.16) is valid only for $\gamma > \gamma_{min}$ where γ_{min} is roughly given by

$$\gamma_{min} \sim \frac{\Omega mc^3}{e^2 \omega_B^2 \sin^2 \theta}. \quad (18.19)$$

Such a γ_{min} corresponds to a lower energy spectral break in the photon spectrum at an energy given by

$$E_{min} = 11 \alpha^9 P_{-1}^7 B_{12}^{-3} \sin^{-3} \theta \text{ eV}. \quad (18.20)$$

Therefore, the distribution of the secondary pairs can be approximated by

$$N_e(\gamma) \sim \begin{cases} \gamma^{-2} \ln(\gamma_{max}/\gamma), & \gamma_{min} \leq \gamma \leq \gamma_{max}, \\ 0, & \gamma < \gamma_{min}. \end{cases} \quad (18.21)$$

Here, we have assumed that no e^-/e^+ is created below γ_{min} .

The pulsed radiation spectrum from a Vela-type outer gap is calculated by using the e^\pm pair distribution of (18.21) with the single particle synchrotron radiation spectrum,

$$\frac{d^2 N_\gamma}{dE_\gamma dt} \propto \frac{1}{E_\gamma} \int_{\gamma_{min}}^{\gamma_{max}} d\gamma N_e(\gamma) F(x), \quad (18.22)$$

where $F(x) = x \int_x^\infty K_{5/3}(y) dy$ with $K_{5/3}$ the modified Bessel function, whose values and asymptotic form are given by [38], and $x = E_\gamma/E_{syn}$ with $E_{syn} = 3\gamma^2 \sin \theta \hbar \omega_B/2$.

18.5.2 A Self-Consistent Outer Gap Model

Pulsars are rapidly rotating, strongly magnetized, neutron stars surrounded by co-rotating plasma up to the light cylinder (R_L , where the co-rotating speed is c). Detailed discussions of the structure of pulsar magnetospheres can be found, for example, in [69] and [9]. It is generally believed that pulsed gamma-rays are emitted within the light cylinder. There are two popular classes of charged accelerator models, i.e., polar cap models (e.g., [32, 47]) and outer gap models. Here we will focus on the outer gap models.

Cheng et al. [18] proposed a two-dimensional outer gap model to explain the observed data of the Crab and Vela pulsars. Their model assumed that the radiation regions are thin in the longitudinal direction. Their double peak γ -ray structure was from two topologically disconnected outer gaps, each of which is associated with different magnetic poles. However, Romani and co-workers [29, 79] have shown that only one outer gap with only outgoing current can already produce a broad, irregularly-shaped emission beam of which is particularly dense near the edge, so that two γ -ray peaks would be observed when the line of sight from the Earth crosses these enhanced γ -ray beam regions; the inner region of the beam provided a significant amount of emission between the peaks. Cheng et al. [20], (hereafter CRZ) have re-considered the three-dimensional magnetospheric gap model by introducing various physical processes (including pair production which depends sensitively on the local electric field and the local radius of curvature, surface field structure, reflection of e^\pm pairs because of mirroring and resonant scattering) to determine the three-dimensional geometry of the outer gap. They have shown that two outer gaps and both outgoing and incoming currents are in principle allowed, but it turns out that outgoing currents dominate the emitted radiation intensities. According to CRZ, the azimuthal extension of the outer gap ($\Delta\Phi \sim 160^\circ$ for the Crab pulsar) is finite and is determined by the local pair production condition. According to [104], the size of the outer gap (f_0) is limited by the pair production between the soft thermal X-rays from the stellar surface and the curvature photons with energy $E_\gamma(f_0)$ emitted by the primary electrons/positrons accelerated in the outer gap. Furthermore, the energy of the soft X-ray photons is determined by the back-flow of the primary electrons/positrons, therefore the soft X-ray energy $E_X(f_0)$ is also a function of the gap size. Using $E_X(f_0)E_\gamma(f_0) \sim (mc^2)^2$, the size of the outer gap can be expressed as

$$f_0 = 5.5P^{26/21}B_{12}^{-4/7}, \quad (18.23)$$

where, $f_0 \leq 1$ is the ratio between the outer gap volume $\sim R_L^3$, $R_L = cP/2\pi$ is the light cylinder radius, P is pulsar period in seconds and B_{12} is the surface magnetic field in units of 10^{12} G. It should be emphasized that $f_0 \leq 1$ otherwise the outer gap does not exist. Zhang et al. [105] have considered how the inclination angle (α) can affect the outer gap size. They find that the size of outer gap will increase for larger inclination angle. The maximum change can be near 75%.

Furthermore, the return particles emit curvature photons with typical energy $E_\gamma = (3/2)(c/s)\hbar\gamma(x)^3$, where $x = s/R_L$, s is the local radius of curvature and

$\gamma(x) \approx 2 \times 10^7 f_s^{1/2} B_{12}^{1/4} P^{-1/4} x^{-3/4}$ [26]. These photons will be converted into the secondary pairs by the neutron star magnetic field if the pair production condition in strong magnetic field is satisfied. From this condition and assuming the local field is dipole field, then the distance to the star of the first generation of e^\pm pairs can be given by [17] $r_s/R = (15E_\gamma B_s / (2mc^2 B_g))^{1/3}$, where B_s is the surface magnetic field and $B_g = m_e^2 c^3 / e\hbar = 4.4 \times 10^{13}$ G. These secondary pairs will lose their energy via synchrotron radiation with the following typical energy $E_{syn} = E_\gamma/20$. Since these synchrotron photons are emitted toward the star, they will encounter stronger magnetic field and convert into e^\pm pairs which again radiate their energy via synchrotron radiation. We can easily show that each new generation of e^\pm pairs will reduce their energy by a factor of ~ 0.05 and comes closer to the star by a factor of ~ 0.37 [17]. The synchrotron spectral index starts with -1.5 and evolves to become -1.9 . We argue that an electromagnetic cascade will take place until the energy of synchrotron photons is ~ 1 MeV and the spectral index ~ -2 . Therefore, the expected X-ray spectrum for $E_X < \text{MeV}$, which consists of soft thermal X-rays and hard non-thermal X-rays, is given by

$$\frac{d\dot{N}_X}{dE_X} = F_{bb}(T_s, E_X) + AE_X^{-2}, \quad (18.24)$$

where F_{bb} is the blackbody spectrum with a characteristic temperature $kT_s = E_X^s$, which satisfies $\int F_{bb} E_X dE_X = L_X^{soft}$ and $A \approx 1.7 \times 10^{35} f^{1/2} P^{-65/12} B_{12}^{29/12} \tan^4 \alpha / \ln(\text{MeV}/\hbar e B(r_s)/mc)$, where r_s is the distance to the star at which the magnetic field becomes strong enough to convert the curvature photons into pairs. We can see that the X-rays consist of two components. Therefore when we fit a finite energy range in X-rays by a simple power law, the photon index could vary for different energy range. Cheng and Zhang [26] have found that the model predicted photon index in the energy range from 100 eV to 2.4 keV is ~ 1 whereas the photon index in the energy range from 2–10 keV is ~ 1.15 , which is only slight steeper than the softer energy band. In fact, they argue that X-ray emission from rotation-powered pulsars in general consist of one non-thermal component, two hard thermal components, and one soft thermal component. The non-thermal X-rays come from synchrotron radiation of e^\pm pairs created in the strong magnetic field near the neutron star surface by curvature photons emitted by charged particles on their way from the outer gap to the neutron star surface. The first hard thermal X-ray component results from polar-cap heating by the return current in polar gap. The second hard thermal X-ray component results from polar-cap heating by the return particles from the outer gap. Because of cyclotron resonance scattering, most of the hard thermal X-rays will be effectively reflected back to the stellar surface and eventually re-emitted as soft thermal X-rays. However, some of the hard thermal X-rays can still escape along the open magnetic field lines, where the e^\pm pair density is low. Furthermore, the characteristic blackbody temperatures of the two hard X-ray components emitted from the polar-cap area inside the polar gap and the polar cap area defined by the footprints of the outer-gap magnetic field lines are strongly affected by the surface magnetic field, which can be much larger than the dipolar field. In fact, the strong

surface magnetic field can explain why the effective blackbody radiation area is nearly two orders of magnitude larger than that deduced from the dipolar field for young pulsars (two orders of magnitude less for old pulsars). However, how many components can be observed depend on the magnetic inclination angle and viewing angle. Their model can explain the observed X-ray spectra from Geminga, PSR B1055–52, PSR B0656+14, and PSR B1929+10 very well. Unlike those two hard thermal X-ray components, which can only be observed in a small solid angle, the non-thermal component and the soft thermal component can cover a much larger solid angle and they are also the strongest components. Therefore (18.24) should be the most likely observed X-ray spectrum.

18.5.3 Single Gap Models

After studying the γ -ray production and light curves for various magnetosphere geometries based on the CHR model, [28] assumed that gap-type regions could be supported along all field lines which define the boundary between the closed region and open field line region rather than just on the bundle of field lines lying in the plane containing the rotation and magnetic dipole axes. In this case, photons are generated which travel tangential to the local magnetic field lines, and there are beams in both the outward (away from the neutron star) and inward directions, because the accelerating gaps are populated by pair production. They considered the pulse profile of radiation produced in the outer gap and showed that a single pole will produce a broad, irregularly-shaped, emission which is particularly dense near the edge. As a result, double γ -ray pulses will be observed when the line of sight from the Earth crosses these enhanced regions of the γ -ray beam, while the inner region of the beam provides a significant amount of emission between the pulses. With a proper choice of the observer viewing angle, a wide range of peak phase separations can be accommodated. Furthermore, [29] refined the calculation of high energy emission from the rotation-powered pulsars based on the CHR model. Their major refinements include (1) the approximate location of the emission at each point in phase along a given line of sight was inferred by using a pulse phase map, and (2) because the spectral emissivities at different emission points will differ, so the outer gap is divided into small sub-zones in the plane containing the rotation and dipole axes. The photon densities and beaming directions for different zone are also different, in which case the particle transport needs to be considered. Under their refinements, they found that the spectral variation of the γ -radiation over the pulsar period is the result of the different emission processes which play a role throughout the outer magnetosphere, however, they were not able to obtain a self-consistent spectrum which resembled the observed high energy spectra, and they attributed this shortcoming to the inability to model appropriately the extremely complex emission processes and their interactions.

Romani and Yadigaroglu [79] modeled the emission geometry and calculated the pulse profile from the single pole outer gap, including the full effects of aberration,

retarded potential and time-of-flight across the magnetosphere. In their model, the radio to γ -ray pulse offset of the known pulsars, and the shapes of the high energy pulse profiles, were determined by using the knowledge of inclination angle α and viewing angle ζ . They gave a range of α and ζ for γ -rays from a pulsar which can be detected at the Earth, and showed that the values of α and ζ for the known γ -ray pulsars can be chosen within observational constraints which not only fall within the parameter space required for γ -ray observability but can explain the measured phase profile offsets and phase separations. Their results indicate that the phase offset is inversely related to the phase separation, and that γ -ray emission can only be observed from pulsars for which the viewing angle is large ($\zeta \geq 45^\circ$), while nearly aligned pulsars ($\alpha \leq 35^\circ$) with their radio emission pointed toward the Earth will have their γ -ray emission beamed away from the Earth (for example PSR B0656+14). Based on this model, Yadigaroglu and Romani [101] calculated the variation of the beaming fraction as a function of the efficiency of high energy γ -ray production. They argued that as the pulsar slows down, the gap should widen and the distance between the last closed field lines and the radiating surface should increase, so more of the open field lines occupy the gap, which implies that older pulsars have larger gaps and will be more efficient at producing \sim GeV γ -rays. Moreover, high energy photons from the outer gaps are primarily radiated along the upper surface of the vacuum gap [29], so a broader outer gap will produce emission closer to the dipole axis. Therefore, the γ -ray beaming solid angle is smaller for an old pulsar. Yadigaroglu and Romani [101] used the fact that the efficiency should increase with age and the observed values of PSR B1706–44 and PSR B1055–52 to derive a phenomenological scaling law for all high energy pulsed emission

$$\eta_\gamma = 3.2 \times 10^{-5} \tau^{0.76}, \quad (18.25)$$

with the characteristic age τ in years. The cut-off to this evolution occurs as the beaming factor drops to zero at $\sim 10^6$ yr.

Romani [78] described a revised picture of gap closure and an emission model for γ -ray pulsars based on curvature radiation reaction-limited charges in the outer magnetosphere. In this model, the following assumptions are made: (1) there is a gap which start near the intersection of the null charge surface and the surface of last closed field lines for which particles can rotate with the star, where the acceleration electric field $E_{\parallel} \sim r^{-1}$; (2) charges are created in this gap and a modest fraction of the local corotation charge density $n_{GJ} = 7 \times 10^8 B_z(r)/P \text{ cm}^{-3}$ experiences this acceleration field, these charges are limited by curvature radiation to $\gamma_{lim} = (eE_{\parallel}/5.6 \times 10^{-3} mc)^{1/4}/s^{1/2}$ and emit curvature photons with a typical energy $E_c \propto \gamma^3/s$, which comprise the main observed EGRET spectrum of the γ -ray pulsars; (3) the gap is maintained by photon-photon pair production, in which soft photons come from the thermal surface emission of the neutron star, with an evolutionary temperature $T(t) = 10^6 (t/10^5)^{-0.05} \exp(-t/10^6)$ K, where time t is in units of years. Because the primaries each radiate $n_\gamma \approx eE_{\parallel} R_L / 2E_c$ photons in transversing the outer gap and the optical depth for primary photons traveling through the magnetosphere is small ($\leq 10^{-3}$ to 10^{-2}), the bulk of the primary flux escapes to

produce the observed beams, but a small fraction of the n_γ primary photons produced by each primary charge produces pairs in the gap, and (4) the electron energy spectrum in the gap is $dN_e/dE_e \propto E_e^{-p}$ with $p = 4$, which causes a curvature spectrum with a spectral index ~ -1.7 extending from $E_c \sim 3$ GeV down to ~ 20 MeV for parameters similar to Vela's. Moreover, since photons are aberrated across field lines, pairs are initially produced with a significant pitch angle ~ 0.1 radian and the pairs near the null charge line will emit synchrotron radiation with a typical energy $E_{syn} \sim 2$ MeV for Vela parameters. Obviously, one of the key quantities in this model is the fractional width of the gap, Romani estimated it by calculating the pair multiplication $n_{mul} = n_\gamma n_2 \sigma_\gamma r_i$, where, n_2 is the soft photon density above threshold and r_i is the radius of the gap closure point. He also estimated the efficiency for GeV photon production and the γ -ray beaming fraction, which are functions of the fractional width of the gap. This model produces phase-resolved GeV spectra for Vela-like parameters which are consistent with those observed by EGRET.

18.5.4 CRZ Model

Cheng et al. [20], (hereafter CRZ) re-consider the three-dimensional magnetospheric outer gap model, following the important ground-breaking work of Romani and co-workers. But instead of assuming a *single* outer gap with *only* an outgoing current, and no restriction on azimuthal directions, they use various physical processes (including pair production which depends sensitively on the local electric field and the local radius of curvature, surface field structure, reflection of e^\pm pairs because of mirroring and resonant scattering) to determine the three-dimensional geometry of the outer gap. In their model, two outer gaps and both outgoing and incoming currents are in principle allowed, but it turns out that outgoing currents dominate the emitted radiation intensities. Furthermore, the three-dimensional structure of outer gaps is completely determined by pair production conditions. Since the potential drop of the gap is

$$\Delta V \approx 6.6 \times 10^{12} f_0^2 B_{12} P^{-2} \text{ V}, \quad (18.26)$$

where $f_0 = h(\langle r \rangle)/R_L$, $h(\langle r \rangle)$ is the average width of the gap boundaries in the (Ω, μ) plane and $R_L = c/\Omega$ is the light cylinder radius, and $\langle r \rangle$ is the average distance to the gap; its value depends on magnetic inclination angle α ($\langle r \rangle \sim R_L/2$). The particle current passing through the gap is

$$\dot{N}_{gap} = 3 \times 10^{30} f_0 \xi B_{12} P^{-2} \text{ s}^{-1}, \quad (18.27)$$

where $\xi = \Delta\phi/2\pi$; $\Delta\phi$ is the transverse extension of the gap. Each of the charged particles inside the gap will radiate high-energy curvature photons with a characteristic energy

$$E_\gamma(f_0) = 2 \times 10^8 f_0^{3/2} B_{12}^{3/4} P^{-7/4} \text{ eV}. \quad (18.28)$$

About half of \dot{N}_{gap} will move toward the star. Although they continue to radiate their energies on the way to the star, they still carry $10.5P^{1/3}$ erg of energy on to the stellar surface. The energy will be radiated back out in hard X-rays. However, resonant scattering with pairs near the star may reflect hard X-rays back to the stellar surface [17, 98], to be re-emitted as soft X-rays with a temperature

$$T_s \approx 3.8 \times 10^6 f_0^{1/4} \xi^{1/4} B_{12}^{1/2} P^{-5/12} \text{ K}. \quad (18.29)$$

The X-ray photon density is very low but each pair produced by an X-ray-curvature photon collisions in the outer gap will emit almost 10^5 curvature γ -rays for further pair creation in that gap. Once the pair production threshold condition $kT_s E_\gamma \geq (m_e c^2)^2$ is satisfied, the gap is unlikely to grow much larger. This pair production condition gives

$$f_0 = 5.5 P^{26/21} B_{12}^{-4/7} \xi^{1/7}. \quad (18.30)$$

Here, ξ is still an unknown quantity. However, f_0 is weakly dependent on ξ which is likely of order of unity. In first approximation, they assume $f_0 = 5.5 P^{26/21} B_{12}^{-4/7}$ [104]. To determine ξ , they consider local pair production processes. The pair production per unit length inside the gap is a decreasing function of r . According to [18], $E_{||} \propto r^{-1/2}$ for the thin outer gap (e.g., the Crab pulsar), which gives $E_\gamma(r) \propto r^{-1/8}$ after using the large r limit $s(r) = (rR_L)^{1/2}$. Since E_γ is only weakly dependent on r , they assume $\sigma_{\gamma\gamma} \approx \text{const.}$

The local pair production per unit length is

$$N_{e^\pm}(r) = (1 - e^{-\tau_{\gamma\gamma}}) N_\gamma(r) \approx \tau_{\gamma\gamma} N_\gamma(r), \quad (18.31)$$

where $\tau_{\gamma\gamma} = n_X(r) \sigma_{\gamma\gamma} l(r)$ is the local optical depth, $n_X = R^2 T_s^4 \sigma / r^2 k T_s c$ is the X-ray number density at r , $l(r) \approx (2s(r)f(r)R_L)^{1/2}$ is the local optical path, $f(r) = h(r)/R_L$ is the local vertical extension of the gap (since $B(r)h^2(r)$ is a constant, which gives $f(r) \propto r^{3/2}$ and $f_0 \sim f(R_L/2)$), and $N_\gamma = eE_{||}(r)/E_\gamma(r)$ is the number of curvature photons emitted at r per e^+/e^- per unit length. Then

$$N_{e^\pm}(r) \propto r^{-11/8}. \quad (18.32)$$

Since most pairs are produced near the null surface where $r = r_{in}$, so the pair production take place mainly in the range $r_{in} \leq r \leq r_{lim}$ where r_{lim} is estimated as $r_{lim} N_{e^\pm}(r_{lim}) / r_{in} N_{e^\pm}(r_{in}) \sim (r_{lim}/r_{in})^{-3/8} \sim 1/2$, which gives $r_{lim} \sim 6r_{in}$. This limits pair production both along the field lines and in transverse directions, and gives

$$\Delta\Phi \sim 160^\circ. \quad (18.33)$$

Within the pair production regions, outgoing and incoming directions for particle flows are allowed. For $r > r_{lim}$ only outgoing current is possible.

The total gamma-ray luminosity is given by $L_\gamma = f_0^3 \dot{E}$, where \dot{E} is the spin-down power of pulsar or it can be expressed as

$$L_\gamma \approx 3.6 \times 10^{31} f^3 B_{12}^2 P^{-4} \text{ erg s}^{-1}. \quad (18.34)$$

The radiation spectrum produced by the primary particles with power-law distribution through synchro-curvature radiation [25] in the outer gap has been obtained by [104]. Therefore, the differential flux at the earth is given by

$$F(E_\gamma) = \frac{1}{\Delta\Omega d^2} \frac{d^2 N_\gamma}{dE_\gamma dt}, \quad (18.35)$$

where $\Delta\Omega$ is the solid angle of γ -ray beaming and d is the distance to the pulsar.

Inside the light cylinder, high energy photons will be emitted nearly tangent to the magnetic field lines in the co-rotating frame because of the relativistic $1/\gamma$ beaming inherent in high energy processes unless $|\mathbf{E} \times \mathbf{B}| \sim \mathbf{B}^2$. Then the propagation direction of each emitted photons by relativistic charged particles can be expressed as (ζ, Φ) , where ζ is the polar angle from the rotation axis and Φ is the phase of rotation of the star. Effects of the time of flight and aberration are taken into account. A photon with velocity $\mathbf{u} = (u_x, u_y, u_z)$ along a magnetic field line with a relativistic addition of velocity along the azimuthal angle gives an aberrated emission direction $\mathbf{u}' = (u'_x, u'_y, u'_z)$. The time of flight gives a change of the phase of the rotation of the star. Combining these two effects, and choosing $\Phi = 0$ for radiation in the (x, z) plane from the center of the star, ζ and Φ are given by $\cos \zeta = u'_z$ and $\Phi = -\phi_{u'} - \mathbf{r} \cdot \hat{\mathbf{u}}'$, where $\phi_{u'}$ is the azimuthal angle of $\hat{\mathbf{u}}'$ and \mathbf{r} is the emitting location in units of R_L . In numerical calculation we assume that the radiation comes a layer of magnetic field lines, which can be identified from their footprints on the polar cap surface. First we determine the coordinate values (x_0, y_0, z_0) of the last closed field lines at the stellar surface, where should be the lower boundary of the outer gap. Then the coordinate values (x'_0, y'_0, z'_0) for the actual emission region can be determined by using $x'_0 = a_1 x_0$, $y'_0 = a_1 y_0$ and $z'_0 = (1 - (x_0^2 + y_0^2))^{1/2}$ for given value of a_1 .

In panel A of Fig. 18.3, the emission morphology in the (ζ, Φ) plane is shown. For a given observer with a fixed viewing angle ζ , a double-pulsed structure is observed because photons are clustered near two edges of the emission pattern due to the relativistic effects (cf. panel B of Fig. 18.3).

In Fig. 18.3, we can see that this model can only produce radiation between two peaks. However, the observed data of the Crab, Vela and Geminga indicate that the leading wing 1 and the trailing wing 2 are quite strong, and even the intensity in off-pulse cannot be ignored. Hirotani and his co-workers [51, 55] have pointed out that the large current in the outer gap can change the boundary of the outer gap. They solve the set of Maxwell and Boltzmann equations in pulsar magnetospheres and demonstrate the existence of outer-gap accelerators, whose inner boundary position depends the detail of the current flow and it is not necessarily located at the null charge surface. For the gap current lower than 25% of the Goldreich–Julian current, the inner boundary of the outer gap is very close to the null surface [49]. On the other hand if the current is close to the Goldreich–Julian current, the inner boundary can be as close as 10 stellar radii (cf. Fig. 18.4).

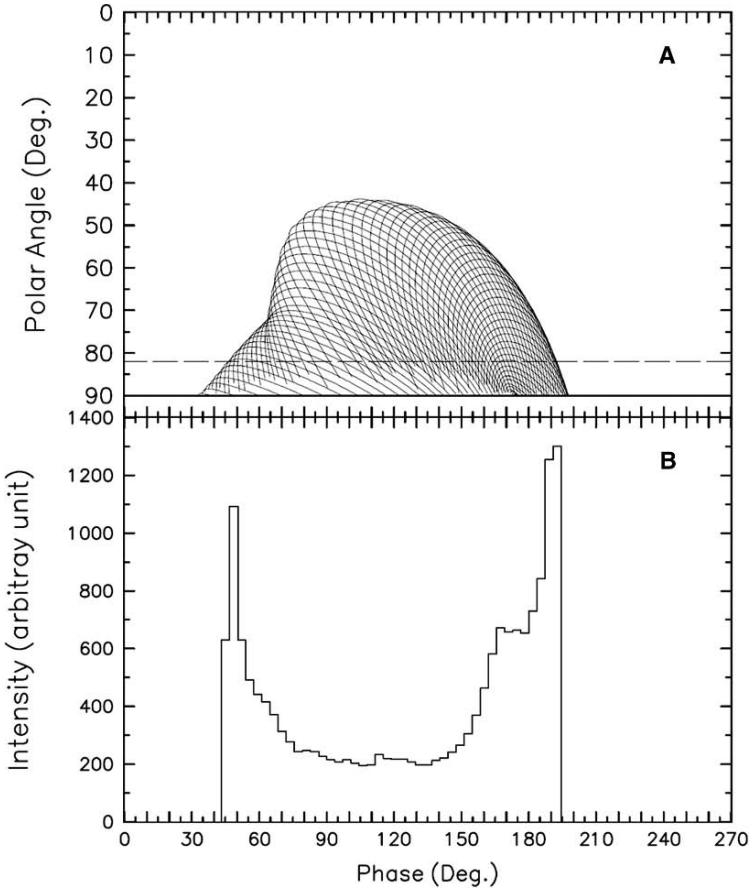


Fig. 18.3 **A** Emission projection onto the (ζ, Φ) plane and **B** pulse profile for the single pole outer gap [20]. The photons are emitted outwards from the outer gap. The choice of parameters are $a_1 = 0.9$, $\alpha = 65^\circ$ and $\zeta = 82^\circ$

In Fig. 18.5, we show the light curve by assuming the inner boundary is extended inward from the null charge surface to 10 stellar radii (cf. panel A of Fig. 18.5). In panel B of Fig. 18.5, the solid line represents emission trajectory of outgoing radiation of gap 1 from the null surface to the light cylinder with $\alpha = 50^\circ$ and $\zeta = 75^\circ$ and the dashed line represents the outgoing radiation from the gap 2 from the inner boundary to the null surface. In the presence of the extended emission region from the near the stellar surface to the null charge surface, leading wing 1, trailing wing 2 and the off-pulse components can be produced. Recently, Takata et al. [91] have also shown that the extension of the outer gap plays a crucial role in explaining the polarization data of the Crab pulsar.

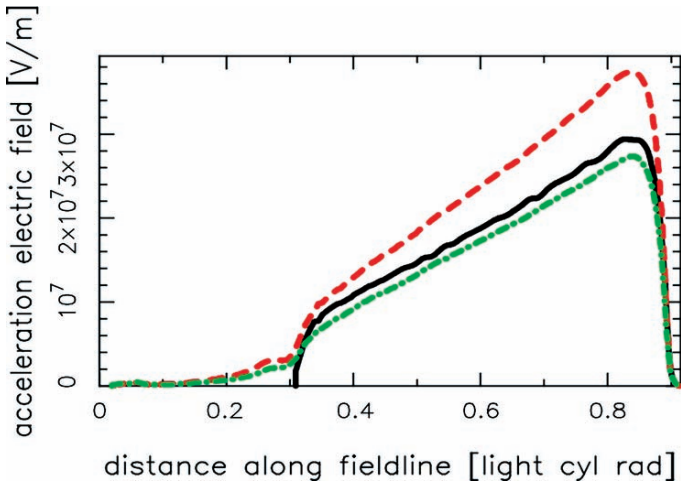


Fig. 18.4 The gap electric field for various intensities of gap current [49]. The *solid line*, the *dashed line* and the *dot-dashed line* are 25%, 50% and 75% of Goldreich–Julian current. The null charge surface is located at $\sim 0.3r_L$

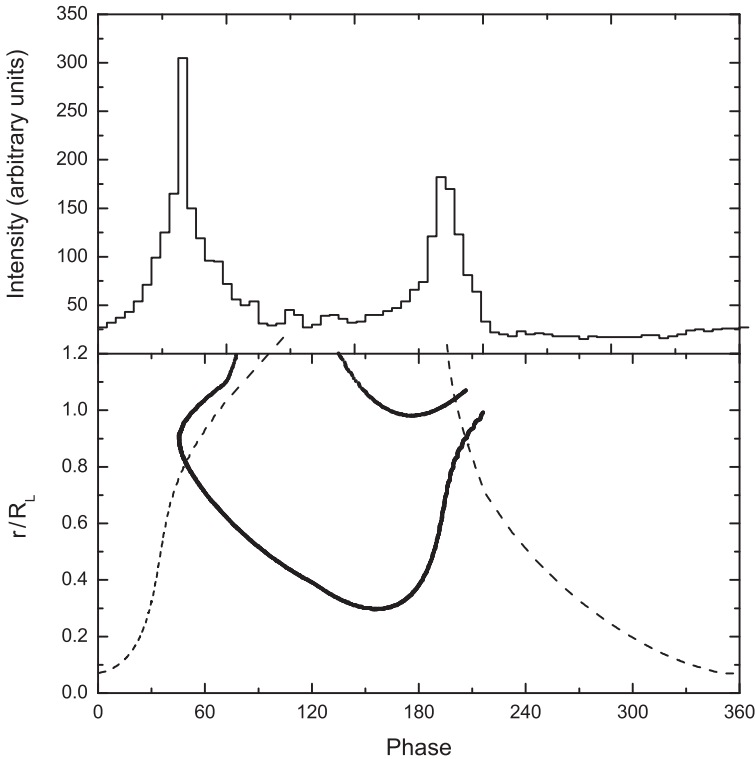


Fig. 18.5 *Upper panel*: the simulated pulse profile of the Crab pulsar; *lower panel*: variation of radial distance with pulse phase for the Crab pulsar in units of R_L , where the *bold line* represents those in the outer magnetosphere, and the *dashed line* represents those in the inner magnetosphere. The inclination angle is 50° and the viewing angle is 75° [60]

18.6 Model Fitting of the Radiation from the Crab Pulsar

In this section, we intend to use the three-dimensional outer gap models introduced in last section to explain the phase-resolved spectrum and the polarization properties of the Crab pulsar.

18.6.1 Phase-Resolved Spectrum of the Crab Pulsar

The Crab pulsar has been studied from the radio to the extremely high energy ranges, and the phase of the double-pulse with separation of 144° is found to be consistent over all wavelengths. Recent observations from COMPTEL and EGRET [64, 95] made it possible to study the phase-resolved properties of the Crab pulsar in γ -ray energies, which indicated that the radiations are from different regions inside the pulsar magnetosphere and phase-resolved spectra are locally dependent. Fierro et al. [36] divided the whole phase into eight intervals, i.e., two peaks, two leading and trailing wings, the bridge between the peaks, and the off-pulse, and we will follow this definition in this paper.

The phase-resolved properties provide more clues and constraints for the theoretical models. So far, the three-dimensional outer gap model seems the most successful model in explaining both the double-peak pulse profile and the phase-resolved spectra of the Crab pulsar (CRZ). However, the leading-edge and trailing-edge of the light curve cannot be given out, since the inner boundary of the outer gap is located at the null charge surface in this model. Recently, the electro-dynamics of the pulsar magnetosphere has been studied carefully by solving the Poisson equation for electrostatic potential and the Boltzmann equations for electrons/positrons [49, 52–54], and the inner boundary of the gap is shown to be located at several stellar radii from the star.

Here, we use the synchrotron self-Compton mechanism (e.g., [24]) to describe the high energy emission from the Crab pulsar.

The electric field of a thin outer gap (CHR) is

$$E_{\parallel}(r) = \frac{\Omega B(r) h^2(r)}{cs(r)} = \frac{\Omega B(r) f^2(r) R_L^2}{cs(r)}, \quad (18.36)$$

where $h(r)$ is the width of the outer gap at position r , and $f(r) = h(r)/R_L$ is the local fractional size of the outer gap. Assuming that the magnetic flux subtended in the outer gap is constant in the steady state, we get the local size factor

$$f(r) \sim f(R_L) \left(\frac{r}{R_L}\right)^{3/2}, \quad (18.37)$$

where $f(R_L)$ is estimated by the pair production condition discussed in the last chapter. As the equilibrium between the energy loss in radiation and gain from

accelerating electric field, the local Lorentz factor of the electrons/positrons in the outer gap is

$$\gamma_e(r) = \left(\frac{3}{2} \frac{s^2}{e^2 c} eE_{\parallel}(r)c \right)^{1/4}. \quad (18.38)$$

For a volume element ΔV in the outer gap, the number of primary charged particles can be roughly written as

$$dN = n_{\text{GJ}} \Delta A \Delta l, \quad (18.39)$$

where $n_{\text{GJ}} = \frac{\Omega \mathbf{B}}{2\pi e c}$ is the local Goldreich–Julian number density, $B\Delta A$ is the magnetic flux through the accelerator and Δl is the path length along its magnetic field lines. Thus, the total number of the charged particles in the outer gap is

$$N \sim \frac{\Omega \Phi}{4\pi c e} R_L, \quad (18.40)$$

where $\Phi \sim f(R_L)B(R_L)R_L^2\Delta\phi$ is the angular range of the outer gap extending along the azimuthal direction. The primary e^{\pm} pairs radiate curvature photons with a characteristic energy

$$E_{\text{cur}}(r) = \frac{3}{2} \hbar \gamma_e^3(r) \frac{c}{s(r)}, \quad (18.41)$$

and the power into curvature radiation for dN e^{\pm} pairs in a unit volume is

$$\frac{dL_{\text{cur}}}{dV} \approx l_{\text{cur}} n_{\text{GJ}}(r), \quad (18.42)$$

where $l_{\text{cur}} = eE_{\parallel}c$ is the local power into the curvature radiation from a single electron/positron. The spectrum of primary photons from a unit volume is

$$\frac{d^2 \dot{N}}{dV dE_{\gamma}} \approx \frac{l_{\text{cur}} n_{\text{GJ}}}{E_{\text{cur}}} \frac{1}{E_{\gamma}}, \quad E_{\gamma} \leq E_{\text{cur}}. \quad (18.43)$$

These primary curvature photons collide with the soft photons produced by synchrotron radiation of the secondary e^{\pm} pairs, and produce the secondary e^{\pm} pairs by photon-photon production. In a steady state, the distribution of secondary electrons/positrons in a unit volume is

$$\frac{d^2 N}{dV dE_e} \approx \frac{1}{\dot{E}_e} \int \frac{d^2 \dot{N}(E'_{\gamma} = 2E'_e)}{dV dE_{\gamma}} dE'_e \approx \frac{1}{\dot{E}_e} \frac{l_{\text{cur}} n_{\text{GJ}}}{E_{\text{cur}}} \ln\left(\frac{E_{\text{cur}}}{E_e}\right), \quad (18.44)$$

with \dot{E}_e the electron energy loss into synchrotron radiation, which is

$$\dot{E}_e = -\frac{2}{3} \frac{e^4 B^2(r) \sin^2 \beta(r)}{m_e^2 c^3} \left(\frac{E_e}{m_e c^2} \right)^2, \quad (18.45)$$

where $B(r)$ is the local magnetic field and $\beta(r)$ the local pitch angle,

$$\sin\beta(r) \sim \sin\beta(R_L)\left(\frac{r}{R_L}\right)^{1/2}, \quad (18.46)$$

$\sin\beta(R_L)$ is the pitch angle at the light cylinder. Therefore, the energy distribution of the secondary electrons/positrons in volume $\Delta V(r)$ can be written as

$$\frac{dN(r)}{dE_e} \approx \frac{d^2N}{dVdE_e}\Delta V(r) \sim \frac{1}{E_e} \frac{l_{cur}n_{GJ}\Delta V(r)}{E_{cur}} \ln\left(\frac{E_{cur}}{E_e}\right). \quad (18.47)$$

The corresponding photon spectrum of the synchrotron radiation is

$$F_{syn}(E_\gamma, r) = \frac{\sqrt{3}e^3B(r)\sin\beta}{m_e c^2 h} \frac{1}{E_\gamma} \int_{E_{min}}^{E_{max}} \frac{dN(r)}{dE_e} F(x) dE_e, \quad (18.48)$$

where $x = E_\gamma/E_{syn}$, and

$$E_{syn}(r) = \frac{3}{2} \left(\frac{E_e}{m_e c^2}\right)^2 \frac{h e B(r) \sin\beta(r)}{m_e c} \quad (18.49)$$

is the typical photon energy, and $F(x) = x \int_x^\infty K_{5/3}(y) dy$, where $K_{5/3}(y)$ is the modified Bessel function of order $5/3$. Also, the spectrum of the inverse Compton scattered photons in the volume $\Delta V(r)$ is

$$F_{ICS}(E_\gamma, r) = \int_{E_{min}}^{E_{max}} \frac{dN(r)}{dE_e} \frac{d^2N_{ICS}(r)}{dE_\gamma dt} dE_e, \quad (18.50)$$

where

$$\frac{d^2N_{ICS}(r)}{dE_\gamma dt} = \int_{\epsilon_1}^{\epsilon_2} n_{syn}(\epsilon, r) F(\epsilon, E_\gamma, E_e) d\epsilon, \quad (18.51)$$

and

$$F(\epsilon, E_\gamma, E_e) = \frac{3\sigma_{TC}}{4(E_e/mc^2)^2} \times \frac{1}{\epsilon} \left[2q \ln q + (1+2q)(1-q) + \frac{(\Gamma q)^2(1-q)}{2(1+\Gamma q)} \right], \quad (18.52)$$

where $\Gamma = 4\epsilon(E_e/m_e c^2)/m_e c^2$, $q = E_1/\Gamma(1-E_1)$ with $E_1 = E_\gamma/E_e$ and $1/4(E_e/m_e c^2) < q < 1$. The number density of the synchrotron photons with energy ϵ is

$$n_{syn}(\epsilon, r) = \frac{F_{syn}(\epsilon)}{cr^2 \Delta\Omega}, \quad (18.53)$$

where F_{syn} is the calculated synchrotron radiation flux, and $\Delta\Omega$ is the usual beam solid angle.

Figure 18.6 shows the observed data of the phase-resolved spectra from 100 eV to 100 GeV of the Crab pulsar, and the theoretical fitting results calculated by using the synchrotron self-Compton mechanism. The phase intervals are defined by division given by [36], and the amplitude of the spectrum in each phase interval is proportional to the number of photons counted in it. In this fitting, both magnetic poles contribute to the high energy radiation. We allow the properties of the north pole and south pole can be slightly different. The detailed description of fitting procedure is described in [92]. The fitting parameters are given in the figure caption. It is interesting to notice that in TW1, Bridge and LW2 there is a strong component appearing at above GeV. In P2 such component also exists but its intensity is relatively weaker. In fact this component is the survived primary photons emitted from the gap. In order to escape from the pair creation, the primary photons must be produced in regions near the light cylinder and also the local soft photon density is low. Figure 18.5 shows the emission regions of each phase. We can see that TW1, Bridge and LW2 have a relative weak synchrotron component in X-rays (cf. Fig. 18.6) and they also have regions close to light cylinder (cf. Fig. 18.5). Therefore they have a

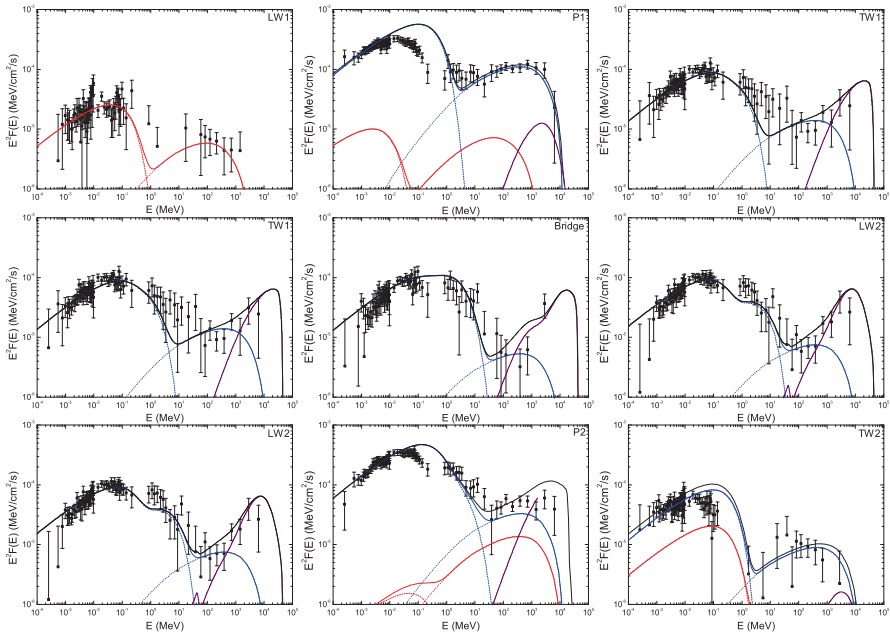


Fig. 18.6 The best model fitting of the phase resolved spectra of the Crab pulsar from 100 eV to 3 GeV in the seven narrow pulse-phase intervals (cf. [92]). Two spectra (for the TW1 and LW2) are displayed twice. The Phase-resolved spectra of the Crab pulsar fitting with $f(R_L) = 0.2$ and 0.3 for the north and the south pole, respectively. $\sin(R_L)$ varies from 0.014 to 0.065. The red and blue colour lines represent the contribution from north and south pole respectively. The black lines in P1, P2 and TW2 are the sum of the contributions from both poles. The fitting curves are compared to the observed data obtained from [64]. The curved line is calculated by the theoretical model, and the observed data are taken from [64]

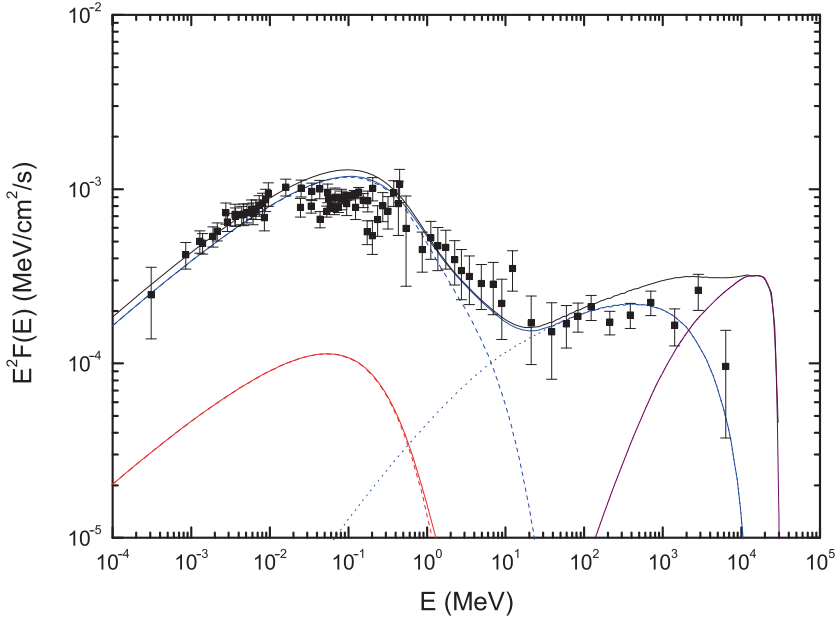


Fig. 18.7 Phase-averaged spectrum of the Crab pulsar. The *dashed line* is the synchrotron radiation and the *dotted line* is the inverse Compton scattering. The observed data are taken from [64]

relatively high survived primary photon component. On the other hand, the emission regions of LW1 and TW2 are always close to star, they do not have much survived primary photons. Both P1 and P2 have very intense X-rays but P2 has part of emission regions very near the light cylinder (cf. Fig. 18.5). The phase-averaged spectrum of the total pulse of the Crab pulsar is shown in Fig. 18.7. In this figure, we can see that the model has over produced the photons around 10 GeV, which seems some improvement is necessary. However, it is important to note that some curvature photons must survive in TW1, Bridge and LW2, which should be robust results.

18.6.2 Polarization of the Crab Pulsar

Takata et al. [91] investigate the polarization of the high-energy emission from the Crab pulsar based on the framework of the three-dimensional outer gap model proposed by [20], they are able to simultaneously reproduce the light curve, the spectrum, and the polarization characteristics by taking into account the gyration of the particles. In order to explain the polarization degree and angle, they conclude that the inner boundary of the outer gap cannot be located at the null charge surface. Instead the inner boundary should be located about 10 stellar radii away from the

neutron star, which is consistent with the previous studies (e.g., [50, 90]). The main reason is that when the pair creation occurs inside the outer gap, the electric field on the null surface can no longer be zero. A new inner boundary can be re-established in a region near the neutron star. The exact location of the inner boundary depends on the exact current flow in the outer gap. Takata et al. [91] has approximated the electric field inside the region from the null surface to the inner boundary by a quadratical form,

$$E_{\parallel} = E_n \frac{(r/r_i)^2 - 1}{(r_n/r_i)^2 - 1}, \tag{18.54}$$

where E_n is the electric field strength at the null charge surface, and r_n and r_i are the radial distances to the null charge surface and the inner boundary respectively.

Then the charged particles are accelerated inside the outer gap and they lose their energy to curvature radiation. However, the curvature photons cannot escape from the light cylinder and they will be converted into secondary electron and positrons. Synchrotron radiation of the secondary pairs produce the optical to soft gamma-rays. Some of gamma-rays will be further converted into tertiary pairs, which are important to contribute the net polarization between two peaks. They calculate the Stokes parameters to obtain the polarization position angle curve and the degree of polarization, which are compared with the Crab optical data (cf. Fig. 18.8). They

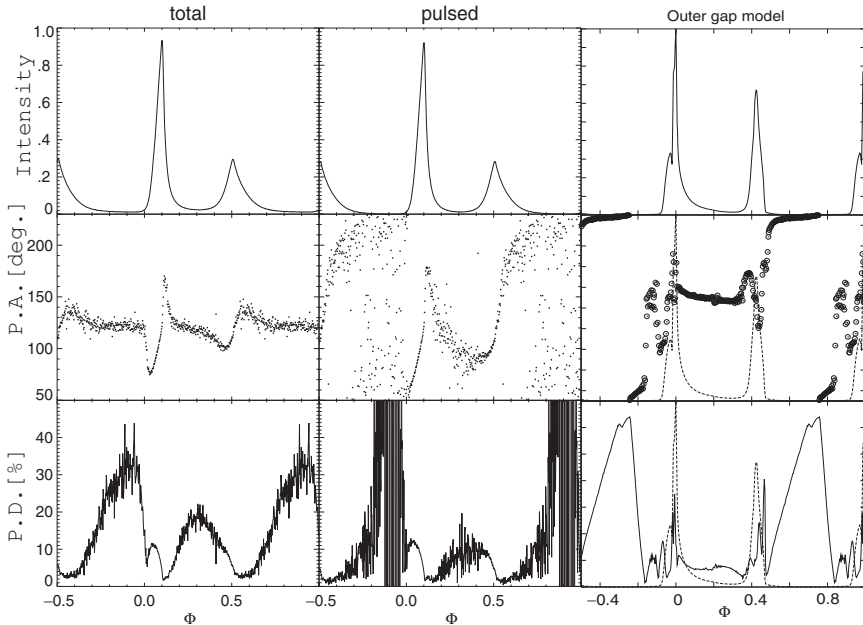


Fig. 18.8 Optical polarization for the Crab pulsar. *Left*, polarization characteristics for the total emission from the pulsar; *middle*, polarization characteristics of the emission after subtraction of the DC level [62]; *right*, predicted polarization characteristics at 1 eV for $\alpha = 50^\circ$, $\zeta = 100^\circ$, and $r_i = 0.67r_n$

demonstrate that the radiation from inside the null charge surface produces the outer wing and off-pulse portions of the light curve and that the tertiary pairs contribute to the bridge emission. The emission from the secondary pairs explains the main features of the observed light curve and spectrum. On the other hand, the emissions both from inside the null charge surface and from the tertiary pairs are required in order to explain the optical polarization behavior of the Crab pulsar. The energy dependence of the polarization features is predicted by the model. From the polarization position angle curve indicates that our viewing angle as measured from the pulsar's rotational axis is greater than 90° .

18.7 A Simple Pulsar Wind Model

The non-thermal radiation can be contributed by the shock wave produced between the pulsar wind and the outflow matter of the companion star (e.g., [88, 93]) or the surrounding nebula (e.g., [27]). In pulsar binaries, the nebula non-thermal emission may be released from the shock front between the pulsar wind and the stellar wind of the companion and interstellar medium (ISM). In this section we introduce simple models to calculate the high energy spectral properties produced from pulsar wind.

Within the theoretical framework, the energy of the electrons is converted to X-ray radiation solely at the shock termination radius. For pulsar motion which is subsonic, the determination of this radius is obtained via the balance between the wind ram pressure and total magnetic and particle pressure within the nebula [76]. In this case, the wind bubble will be nearly centered about the position of the pulsar. Rees and Gunn [76] estimated $R_s \sim 3 \times 10^{17}$ cm, which is consistent with the size of the inner X-ray ring of the Crab nebula (~ 0.1 pc, see [63, 99]). The termination shock picture is not necessarily restricted to slowly moving pulsars since even for pulsars moving at several hundred kilometers per second the motion can be subsonic in, for example, regions where the gas has been heated to temperatures of $\sim 10^8$ K by a supernova shock. The radius of the termination shock can be estimated as

$$R_s \simeq \left(\frac{L_{sd}}{B^2 c} \right)^{1/2} \sim 6 \times 10^{14} L_{sd,34}^{1/2} B_{mG}^{-1} \text{ cm}, \quad (18.55)$$

where $L_{sd,34}$ is the pulsar spin-down power in units of 10^{34} erg s^{-1} and B_{mG} is the magnetic field strength in the nebula in milli-gauss. With the observed values of the Crab pulsar and its nebula ($L_{sd,34} = 5 \times 10^4$ and $B_{mG} = 0.5$), consistency of the shock radius is easily achieved.

For supersonic motion, the nebula will form a bow shock morphology. In this case, the termination shock radius is given by the balance of the ram pressure between the wind particles and the medium at the head of the bow shock:

$$\frac{L_{sd}}{4\pi c R_s^2} = \frac{1}{2} \rho_{ISM} v_p^2, \quad (18.56)$$

where ρ_{ISM} is the density of the interstellar medium and v_p is the pulsar's proper motion velocity. The termination shock radius is given as

$$R_s \simeq \left(\frac{L_{\text{sd}}}{2\pi\rho_{\text{ISM}}v_p^2c} \right)^{1/2} \sim 3 \times 10^{16} L_{\text{sd},34}^{1/2} n_1^{-1/2} v_{p,100}^{-1} \text{ cm}, \quad (18.57)$$

where n_1 , and $v_{p,100}$ are the number density in the interstellar medium in units of 1 particle cm^{-3} and the pulsar space velocity in units of 100 km s^{-1} . For example, [14] recently discovered a bow shock structure coincident with the Geminga pulsar based on observations obtained with *XMM-Newton*. An estimate of the termination radius for Geminga follows from its spin down power, $L_{\text{sd}} \simeq 3.2 \times 10^{34} \text{ erg s}^{-1}$, distance of $\sim 160 \text{ pc}$, and proper motion velocity of $v_p \sim 120 \text{ km s}^{-1}$ [11], leading to a radius of $4 \times 10^{16} \text{ cm}$ which is consistent with the observational constraint on Geminga's compact X-ray nebula.

Generally, assuming the equipartition between the electron energy and magnetic field, i.e., $\epsilon_e \sim \epsilon_B \sim 0.5$, the magnetic field in the emitting region of the shock can be estimated as $B = (6\epsilon_B \dot{E}/R_s^2 c)^{1/2}$. For the strong relativistic shock, the postshock electron energy distribution is $N(\gamma) \propto \gamma^{-p}$ for $\gamma_m < \gamma < \gamma_{\text{max}}$, where $\gamma_m = \frac{p-2}{p-1} \epsilon_e \gamma_w$, γ_w is the Lorentz factor of the relativistic pulsar wind. γ_{max} can be estimated by the equivalence between the electron acceleration time-scale and the synchrotron cooling time-scale. The electron synchrotron cooling time is $t_{\text{syn}} = 6\pi m_e c / \sigma_T \gamma B^2$, the acceleration time is given by $t_{\text{acc}} = \gamma m_e c / eB$, then $\gamma_{\text{max}} = (6\pi e / \sigma_T B)^{1/2}$, where σ_T is the Thompson cross section. So the maximum photon energy emitted by the relativistic electrons is about $E_{\text{max}} \sim \frac{3\hbar e B}{2m_e c} \gamma_{\text{max}}^2 \sim 250 \text{ MeV}$.

The number of radiating particles at γ , $N(\gamma)$, is determined by a balance between the rate at which particles are injected at the shock front $\dot{N}(\gamma)$ and synchrotron losses. The synchrotron power of an electron with γ is $P(\gamma) = \frac{4}{3} \sigma_T c \gamma^2 \frac{B^2}{8\pi}$ and $\dot{N}(\gamma) = (p-1) \gamma_m^{p-1} (\gamma_w m_e c^2)^{-1} \dot{E}_{\text{sd}} \gamma^{-p}$. The balance between injection and synchrotron losses can be expressed as $\frac{1}{m_e c^2} \frac{\partial N(\gamma) P(\gamma)}{\partial \gamma} = \dot{N}(\gamma)$. The solution is $N(\gamma) = \gamma_m^{p-1} (\gamma_w P(\gamma))^{-1} \dot{E} \gamma^{-(p-1)}$. The luminosity of radiating particle in the range from γ to $\gamma + d\gamma$ is $P(\gamma)N(\gamma)$, leading to the luminosity per unit frequency

$$L_\nu = k(p) \gamma_w^{p-2} R_s^{-(p-2)/2} \dot{E}^{(p+2)/4} \nu^{-p/2}, \quad (18.58)$$

when $\nu_X > \nu_c$ is called the fast cooling regime. Here $k(p) = \frac{1}{2} \left(\frac{p-2}{p-1} \right)^{p-1} \left(\frac{6e^2}{4\pi^2 m_e c^3} \right)^{(p-2)/4} \epsilon_e^{p-1} \epsilon_B^{(p-2)/4}$, ν_X is the observed X-ray frequency and ν_c is called the cooling frequency. The determination of the cooling frequency is given as $\nu_c = \frac{e}{2\pi m_e c B^3} \left(\frac{6\pi m_e c}{\sigma_T t} \right)^2$, where t is a characteristic timescale of the nebula estimated as the flow timescale in a characteristic radiation region, i.e., $t \sim R_s / v_p$. For the slow cooling case $\nu_X < \nu_c$, $L_\nu \sim \nu^{-(p-1)/2}$. The luminosity at a particular frequency ν can be estimated as νL_ν . Since $p = 2 \sim 3$, we expect that the photon spectral index of high energy spectrum produced by pulsar wind should be $1.5 \sim 2.5$.

Non-thermal radiation can also arise from a shock wave resulting from the interaction between the pulsar wind and the outflowing matter from the companion

star [5, 88, 93]. In this context, the neutron star is at a distance, D , from the surface of its binary companion given by $D = R + R_s$, where R_s is the shock wave termination radius as measured from the neutron star surface and R is the distance of the shock from the surface of the companion star. For millisecond pulsars in binary systems with low mass companions, we adopt an orbital separation $\sim 2 \times 10^{11}$ cm. If we assume that mass is lost isotropically from the companion star, the loss rate is given as $\dot{M} = 4\pi\rho(R_* + R)^2 v_w$, where v_w is its outflow velocity, ρ is the density at distance R from the stellar surface and R_* is the radius of the companion. The dynamic outflow pressure given by $P_w(R) = \rho(R)v_w(R)^2$ can be expressed as

$$P_w(R) = \frac{\dot{M}v_w}{4\pi(R_* + R)^2}. \quad (18.59)$$

The termination radius of the pulsar wind is given by the pressure balance between the pulsar and companion outflow and can be expressed as

$$\left(\frac{R_s}{R_* + R} \right)^2 = \frac{\dot{E}}{\dot{M}v_w c}. \quad (18.60)$$

In order to estimate the shock radius, \dot{M} and v_w must be determined. Unlike the case of the progenitor of millisecond pulsars, i.e., the low mass X-ray binaries, where \dot{M} can be estimated from the X-ray accretion luminosity, the mass loss rate from the neutron star companion likely results from the evaporation by a pulsar wind [82]. If the stellar wind is a consequence of evaporation by the pulsar wind, the balance between the stellar wind pressure and the pulsar wind pressure lies near the position of the companion, implying $R_s \sim D$. In taking PSR B1957+20 as an example, we find that $R_s > 0.6(R_* + D)$ under the assumption that the wind velocity is comparable to the escape speed from the companion and the mass loss rate is $< 10^{17}$ g s $^{-1}$ (see [87]).

The cooling frequency ν_c is given as $\nu_c = \frac{e}{2\pi m_e c B^3} \left(\frac{6\pi m_e c}{\sigma_T t_f} \right)^2$, where $t_f \sim \sqrt{3}R_s/c$ is the dynamical flow time and the magnetic field strength at the termination radius is estimated by $B = (6\epsilon_B \dot{E}/R_s^2 c)^{1/2}$. Taking $\dot{E} \sim 10^{35}$, $\epsilon_B \sim 0.003$, and $R_s \sim 10^{11}$ cm, we obtain $\nu_c \sim 3 \times 10^{21}$ Hz. Since the cooling frequency is much larger than the frequency $\nu_x \sim 10^{18}$ Hz, the observed luminosity per frequency $L_\nu \propto \nu^{-(p-1)/2}$. Based on the work by [27], the total X-ray luminosity radiated in the intra-binary shock wave for a solid angle of Ω toward the pulsar is estimated as

$$\begin{aligned} \nu L_\nu = & \frac{\Omega}{4\pi} \frac{\sigma_T 6^{(p-3)/4} (p-2)^{p-1}}{2\pi m_e c^{(p+5)/4} (p-1)^{p-2}} \left(\frac{e}{2\pi m_e c} \right)^{(p-3)/2} \epsilon_e^{p-1} \epsilon_B^{(p+1)/4} \\ & \times R_s^{-(p+1)/2} \gamma_w^{p-2} t_f \dot{E}^{(p+5)/4} \nu^{-(p-3)/2}, \end{aligned} \quad (18.61)$$

in the X-ray energy band (2–10 keV). It is interesting to note that if we approximate $t_f \sim \sqrt{3}R_s/c$ and $R_s = D$, the above equation can be rewritten as

$$\nu L_\nu = 5 \times 10^{30} \alpha(p) f_{0.1} D_{11}^{-(p-1)/2} \dot{E}_{35}^{(p+5)/4} \text{ erg s}^{-1}, \quad (18.62)$$

for $\nu = 10^{18}$ Hz, $\gamma_w = 10^6$, $\epsilon_e = 0.5$, $\epsilon_B = 0.003$ and $\alpha(p)$ is a function of p , which only varies from 1 to 2.6 as p increases from 2.2 to 2.6. For simplicity, we may assume it is a constant of order of unity. Here, $f = \Omega/4\pi$, $D_{11} = D/10^{11}$ cm and $\dot{E}_{35} = \dot{E}/10^{35}$ erg s $^{-1}$. We note that [93] have estimated that $\epsilon_B \sim 0.02$ in the intra-binary shock region in order to explain the X-ray emission from PSR 1259–63. For this value, the coefficient in equation (12) will change to 3×10^{31} .

18.8 Applications to X-Ray Emission

18.8.1 L_x – L_{sd} Relations from ASCA Data

Over 50 rotation powered pulsars have been detected in the X-ray band [6], but only a fraction of them have been resolved with pulsed non-thermal components. Here, we have selected 23 X-ray pulsars with both pulsed and non pulsed emission measurements obtained from the ASCA mission (listed in Table 18.1). Our pulsar sample includes 19 normal pulsars and 4 millisecond Pulsars (cf. [22] for the description of data selection). Since the ASCA satellite does not have high spatial resolution,

Table 18.1 Characteristics of spin powered pulsars and their X-ray luminosities observed by ASCA [22]

PSR	P (s)	\dot{P} (s s $^{-1}$)	d	L_{sd}	$L_{X,tot}$	$L_{X,pul}$	$L_{X,npul}$
J0631+1036	0.288	1.0×10^{-13}	1.0	5.4×10^{34}	4.2×10^{31}	2.0×10^{31}	2.2×10^{31}
J1811–1926	0.065	4.4×10^{-14}	5.0	7.0×10^{36}	1.6×10^{34}	1.9×10^{33}	1.4×10^{34}
B0531+21	0.033	4.2×10^{-13}	2.0	4.5×10^{38}	1.1×10^{37}	6.8×10^{35}	1.0×10^{37}
B0833–45	0.089	1.25×10^{-13}	0.3	6.9×10^{36}	1.9×10^{33}	1.5×10^{32}	1.8×10^{33}
B0633+17	0.237	1.1×10^{-14}	0.16	3.2×10^{34}	8.2×10^{29}	4.6×10^{29}	3.6×10^{29}
B1706–44	0.1025	9.3×10^{-14}	1.82	3.4×10^{36}	6.8×10^{32}	4.1×10^{32}	2.7×10^{32}
B1509–58	0.150	1.54×10^{-12}	4.3	1.8×10^{37}	4.0×10^{34}	1.3×10^{34}	2.7×10^{34}
B1951+32	0.0395	5.8×10^{-15}	2.5	3.7×10^{36}	6.2×10^{33}	6.2×10^{32}	5.6×10^{33}
B1046–58	0.124	9.6×10^{-14}	2.98	2.0×10^{36}	9.5×10^{32}	5.5×10^{32}	4.5×10^{32}
B1929+10	0.227	1.16×10^{-15}	0.17	3.9×10^{33}	1.54×10^{30}	5.6×10^{29}	9.8×10^{29}
B0656+14	0.385	5.5×10^{-14}	0.76	3.8×10^{34}	1.7×10^{31}	1.0×10^{31}	7.0×10^{30}
B0540–69	0.05	4.8×10^{-13}	49.4	1.5×10^{38}	8.3×10^{36}	1.3×10^{36}	7.0×10^{36}
B0950+08	0.253	2.3×10^{-16}	0.12	5.6×10^{32}	4.6×10^{29}	1.6×10^{29}	3.0×10^{29}
B1610–50	0.232	4.93×10^{-13}	7.26	1.6×10^{36}	9.6×10^{33}	3.0×10^{33}	6.6×10^{33}
B1055–52	0.197	5.83×10^{-15}	1.53	3.0×10^{34}	2.7×10^{30}	2.0×10^{30}	7.0×10^{29}
B1853+01	0.267	5.4×10^{-13}	2.02	8.0×10^{35}	1.4×10^{33}	1.4×10^{32}	1.3×10^{33}
J2229+6114	0.0516	7.8×10^{-14}	3.0	2.2×10^{37}	1.7×10^{33}	4.0×10^{32}	1.3×10^{33}
B0537–69	0.016	5.13×10^{-14}	47	4.8×10^{38}	2×10^{36}	1.7×10^{35}	1.8×10^{36}
J1846–0258	0.32	7.1×10^{-12}	19	1×10^{37}	1×10^{36}	4×10^{34}	1×10^{36}
B1937+21	0.00156	1.05×10^{-20}	3.6	1.1×10^{36}	5.7×10^{32}	2.5×10^{32}	3.2×10^{32}
J2124–3358	0.005	1.08×10^{-20}	0.25	3.5×10^{33}	4.8×10^{29}	1.6×10^{29}	3.2×10^{29}
B1821–24	0.003	1.6×10^{-18}	5.1	2.2×10^{36}	6.5×10^{33}	9.4×10^{32}	5.5×10^{33}
J0437–47	0.0058	2.0×10^{-20}	0.18	4.2×10^{33}	1.3×10^{30}	4.0×10^{29}	9.0×10^{29}

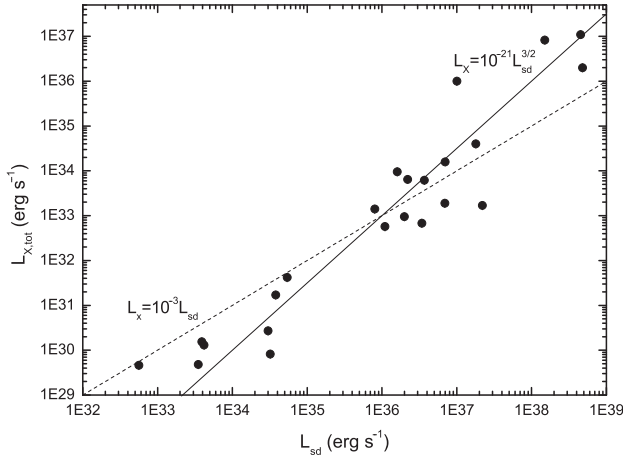


Fig. 18.9 The total X-ray luminosity (2–10 keV) from ASCA observations vs. spin-down power of 23 X-ray pulsars. The *solid line* is $L_x = 10^{-21} L_{sd}^{3/2}$ [84], and the *dashed line* represents $L_x = 10^{-3} L_{sd}$ [7]. The best fitting function is $L_x \propto L_{sd}^{1.35}$

the X-ray luminosity of the pulsars in the ASCA field is composed of emission from the pulsar's magnetosphere and compact pulsar wind nebula. For reference, the total pulsed plus non pulsed X-ray luminosity in the ASCA energy range (2–10 keV) is plotted vs. spin down power in Fig. 18.9. A correlation is found which is consistent with the form $L_x \propto L_{sd}^{1.5}$ found by [84], but the best fit form of this correlation is found to be $L_x \propto L_{sd}^{1.35 \pm 0.2}$. Here, the error in the power law exponent represents $\pm 1\sigma$ corresponding to the scatter in the observed data points, which may reflect variations in ϵ_e , ϵ_B , γ_w , and uncertainties in distance from pulsar to pulsar. Our best fit power law relation is consistent with the conclusion of [74], who used a sample of 39 pulsars observed mainly by ROSAT and data from ASCA, RXTE, BeppoSAX, Chandra and XMM-Newton. Although [74] considered their result ($L_x \propto L_{sd}^{1.34}$) statistically unacceptable, our result is not subject to the uncertainties associated with the normalization of different satellite data to obtain the X-ray luminosity between 2 and 10 keV (cf. Table 18.1 of [74]), for which the extrapolation relied on the uncertain photon index in the ROSAT energy band.

The X-ray luminosity associated with the pulsed emission component is illustrated vs. spin down power in Fig. 18.10. A correlation separate from the total luminosity is found which is inconsistent with either the form $L_x \propto L_{sd}$ or $L_x \propto L_{sd}^{3/2}$. The best fitting function to the data is found to be $L_{X,pul} \simeq (1.0 \pm 0.6) \times 10^{-11} L_{sd}^{1.2 \pm 0.08}$, which significantly deviates from the 3/2 power law relation proposed by [84]. Such a relation is consistent with the relation $L_x \propto L_{sd}^{1.15}$ derived from the theoretical X-ray magnetospheric emission model. However, this latter result is not without uncertainties since the inclination angle of the magnetic field with respect to the rotation axis and the viewing angle is not well determined. The observed conversion efficiencies are found to range from $\sim 10^{-5}$ to 9×10^{-3} , which is not in conflict with model predictions [17, 26].

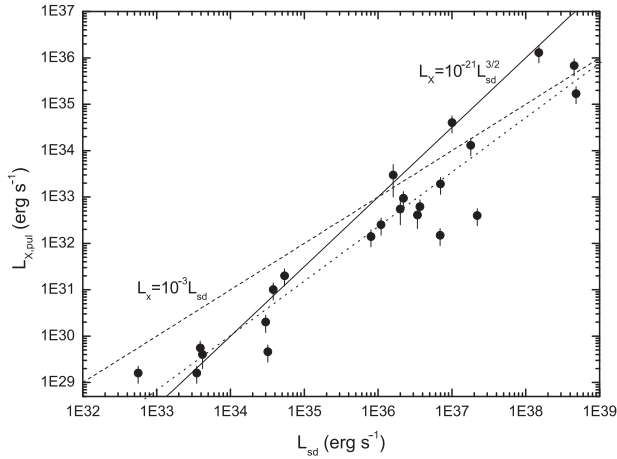


Fig. 18.10 The pulsed X-ray luminosity (2–10 keV) from ASCA observations vs. spin-down power of 23 X-ray pulsars. The *solid line* is $L_X = 10^{-21} L_{sd}^{3/2}$, and the *dashed line* represents $L_X = 10^{-3} L_{sd}$. The relation between the pulsed component and spin-down power cannot be described by both the two formulae. The best fitting function is shown as the *dotted line*, $L_{X,pul} = 10^{-11} L_{sd}^{1.2}$

A correlation is also found to exist between the non pulsed X-ray luminosity and the spin down power as shown in Fig. 18.3 of [22]. The data points are consistent with the previous ASCA relation of the type $L_x \propto L_{sd}^{3/2}$, but the correlation is also consistent with $L_{x,npul} \propto L_{sd}^{1.4 \pm 0.1}$. Upon comparison to the results from Fig. 18.9, this power law relation is a consequence of the fact that the pulsar emission in the ASCA sample is dominated by the non pulsed radiation component. The conversion efficiency for the non pulsed component overlaps with that for the pulsed component, but extends to efficiencies as high as 0.1.

Generally, the X-ray luminosity of pulsar wind nebulae [27] is a nonlinear function of the spin down power. As can be seen in last section, the nebula's X-ray luminosity follows from

$$L_x \propto \varepsilon_e^{p-1} \varepsilon_B^{(p-2)/4} \gamma_w^{p-2} R_s^{-(p-2)/2} L_{sd}^{(p+2)/4}. \quad (18.63)$$

Here, ε_e and ε_B are assumed to be constant, but $R_s \propto L_{sd}^{1/2}$ from (55) and (57). Although the above equation corresponds to the fast cooling regime, the dependence of L_X on L_{sd} for the slow cooling regime is unchanged because the ratio of the X-ray luminosities in these two regimes depends only on the cooling frequency ν_c , which is independent of L_{sd} . We note that γ_w also depends on the spin down power so the explicit dependence of L_x on L_{sd} remains to be theoretically determined. To estimate this dependence we make use of the results of [80] and [2], who argued that large fluxes of protons (ions) could also be extracted from the neutron star and accelerated in the parallel electric field in the magnetosphere. The initial Poynting flux can be converted into particle thermal and kinetic energy well within the termination radius. Since both electrons and protons are basically accelerated

by the low frequency electromagnetic wave generated by the pulsar, they will be accelerated to the same relativistic speed as they are bound by the strong electrostatic force. Hence, the Lorentz factor of the electrons and protons are the same, leading to the result that the protons may have carried away most of the spin down power [30]. Thus, we can obtain a form for the spin down power from

$$L_{sd} \sim \dot{N} \gamma_w m_p c^2, \quad (18.64)$$

where \dot{N} is the outflow current from the surface. This current should be of the order of the Goldreich–Julian current [40] given as $\dot{N} \simeq 1.35 \times 10^{30} B_{12} P^{-2} \text{s}^{-1}$. Since $L_{sd} \simeq 10^{31} B_{12}^2 P^{-4} \text{erg s}^{-1}$, we find $\dot{N} \propto L_{sd}^{1/2}$, leading to $\gamma_w \propto L_{sd}^{1/2}$. Therefore, we obtain the relation $L_x \propto L_{sd}^{p/2}$, where p generally varies between 2 and 3. The relation deduced from the non pulsed X-ray luminosity and spin down power of observed pulsars may result from a relatively high electron energy index in the nebula.

18.8.2 Why Do MSPs in the Field and Those in 47 Tuc Obey Different L_x – L_{sd} Relation?

The discovery of millisecond pulsars (MSPs) as a class of rapidly rotating ($P < 10$ ms), weakly magnetized ($B \lesssim 10^{10}$ G) neutron stars has stimulated considerable interest in the fundamental properties of these objects. The detailed observational study of these sources over periods of time have provided insights into their origin and evolution in close binary systems (see for example, [73]). The hypothesis that MSPs are neutron stars recycled in a spin up phase during which angular momentum and mass are accreted from a companion star [1, 75] has been dramatically confirmed with the observational detection of the four millisecond accreting X-ray pulsars J1808.4–3658 [100], J1751–305 [67], J0929–314 [37], and J1807–294 [66]. Their combination of short spin period and low dipole magnetic field strengths have, furthermore, provided important clues on the temporal evolution of magnetic fields in neutron stars in low mass X-ray binary systems ([97]; see also [10] for a recent review).

Insights into the nature of the emission mechanisms have been facilitated by observational investigations over broad spectral regions. As an example, the early X-ray studies of MSPs using the ROSAT satellite revealed that the MSPs in the Galactic field appear to have a non thermal character (see [7, 8]) with a power law photon index ranging from ~ -2 to -2.4 . On the other hand, the recent X-ray studies with the Chandra satellite by [42] indicate that the MSPs in 47 Tuc appear to be consistent with a thermal blackbody spectrum characterized by a temperature corresponding to an energy of 0.2–0.3 keV.

Additional evidence supporting the apparent difference between the MSPs in the Galactic field and in 47 Tuc and, hence difference in their fundamental properties, can be gleaned from the relation between the X-ray luminosity, L_x , and the spin down power, L_{sd} , expressed in the form $L_x \propto L_{sd}^\beta$. Using ROSAT data [7, 8] found that

$\beta \sim 1$ for MSPs in the Galactic field, whereas there are hints that the dependence is shallower ($\beta \sim 0.5$) for the MSPs in 47 Tuc (see [42]). An existence of a correlation between these two quantities provides strong evidence for relating the energy source of the X-ray emission to the rotational energy of the underlying neutron star. We shall, for convenience, group the MSPs with properties similar to the Galactic field as Type I and those similar to the MSPs in 47 Tuc as Type II, even though the nearest MSP J0437–4715 has an X-ray spectrum consisting of two thermal components and one non thermal component [102].

Despite the fact that these two types of MSPs have similar values in rotation period, orbital period and dipole magnetic field. They have the following differences. X-rays from MSPs in the field is dominated by the non-thermal whereas X-rays from MSPs in 47 Tuc is dominated by thermal component (cf. [41]). Furthermore, there are observation evidence that MSPs in the field with parameters similar to the Crab and the Vela could be gamma-ray sources (cf. [21]). On the other hand, the entire 47 Tuc may contains over hundreds of MSPs but it is not a EGRET source, which implies MSPs in the globular cluster are poor gamma-ray emitters even they have similar parameters as those in the field, why? Form the evolution point of view, even both types of MSPs may be recycle pulsars. Whereas the stellar density in 47 Tuc is much higher. Consequently MSPs in the globular cluster may change their companions a few time during their life time. If accretion can affect the surface magnetic field structure, which is likely the case, MSPs in the globular cluster may have much more complicated field morphology than those in the field. Finally although the spin-down age for both type of MSPs is similar, the true age of MSPs in globular cluster is most likely older than those in the field.

Cheng and Taam [21] have argued that the observed spectra and X-ray luminosities of millisecond pulsars in 47 Tuc can be interpreted in the context of theoretical models based on strong, small scale multipole fields on the neutron star surface. For multipole fields that are relatively strong as compared to the large scale dipole field, the emitted X-rays are thermal and likely result from polar cap heating associated with the return current from the polar gap. On the other hand, for weak multipole fields, the emission is non-thermal and results from synchrotron radiation of e^\pm pairs created by curvature radiation as described by [104]. The X-ray luminosity, L_x , is related to the spin down power, L_{sd} , expressed in the form $L_x \propto L_{sd}^\beta$ with $\beta \sim 0.5$ and ~ 1 for strong and weak multipole fields respectively. If the polar cap size is of the order of the length scale of the multipole field, s , the polar cap temperature is given by

$$T_s \sim 3 \times 10^6 K \left(\frac{L_{sd}}{10^{34} \text{ergs}^{-1}} \right)^{1/8} \left(\frac{s}{3 \times 10^4 \text{cm}} \right)^{-1/2}. \quad (18.65)$$

The main reason why such relation occurs is as follow. The polar cap potential with strong multipole is likely insensitive to pulsar parameters (e.g., [26, 61, 83]). The current flow in the polar cap is limited by the Goldreich and Julian current [40], which is proportional to $L_{sd}^{1/2}$. Therefore the thermal X-ray luminosity L_x resulting from the polar cap heating is simple proportional to $L_{sd}^{1/2}$. The existence of multipole also explains why MSPs in 47 Tuc are poor gamma-ray emitters. According to [81],

Table 18.2 Three types of millisecond pulsars and their X-ray properties

	D (kpc)	n (cm^{-3})	B G	v_p (km s^{-1})	$\delta\theta$	R_{obs} (cm)	R_s (cm)	Spectrum
GC ^a	8.5	10^2	10^{-4}	100	$1''$	6×10^{16}	3×10^{15}	Non-thermal
1957+20	1.5	1	10^{-5}	220	$5''$	6×10^{16}	4×10^{16}	Non-thermal
47 Tuc	5	0.1	10^{-5} – 10^{-6}	60	$1''$	3.5×10^{16}	2×10^{17}	Thermal

^aMillisecond pulsars in the Galactic Center and PSR B1957+20. D is the distance, n is the number density in the medium surrounding the pulsar, B is the magnetic field in the interstellar medium, v_p is the pulsar proper motion velocity, $\delta\theta$ is the detection angular limit in the different observations, $R_{\text{obs}} \sim D\delta\theta/2$ is the radius of the aperture, and R_s is the predicted shock radius. For the Galactic center, we take a spin down power of $2 \times 10^{34} \text{ erg s}^{-1}$ and an average velocity of pulsars of 130 km s^{-1} , which is lower than the escape speed from this region

they argue that complicated surface magnetic field can emit high curvature photons, which subsequently become pairs in those field leading to outer gap. These pairs can quench the outer gap, therefore non-thermal emission originated from this accelerator is missing. But PWNe should contribute to the non-thermal emission. However, in Table 18.2 we show that the typical shock radius in 47 Tuc is smaller than the observed radius by Chandra in order to identify each MSP in 47 Tuc. Therefore the observation will exclude the non-thermal emission from PWNe [23]. We conclude that the X-ray emission from most MSPs in 47 Tuc can be described by thermal X-ray emission with temperature given by above estimation and their $\beta \sim 0.5$.

However, there are some exceptions. For examples the more recent work by [13] on the spectral and long-timescale variability analyses of *Chandra* observations of 18 millisecond pulsars in 47 Tuc has led to the discovery that the three sources, 47 Tuc J, O and W, exhibit a significant non-thermal component. The photon index of these three sources are in the range 1 ± 0.56 , 1.33 ± 0.79 , and 1.36 ± 0.24 respectively. Of these, only 47 W exhibits dramatic X-ray variability as a function of orbital phase. We note that since 47 Tuc O lies near the center of the cluster where the number density of X-ray sources is large its non-thermal spectrum may be contaminated by background sources in the field. Of the remaining two millisecond pulsars, it is possible that the non-thermal spectral components are produced in an intra-binary shock formed by the interaction between the relativistic wind and matter from the stellar companion [13]. Thus, these observations do not suggest a magnetospheric origin for the non thermal emission at such levels. The much higher non-thermal X-ray luminosity from W ($\sim 2.7 \times 10^{31} \text{ erg s}^{-1}$), in comparison to J ($\sim 9.3 \times 10^{30} \text{ erg s}^{-1}$), may reflect the differing nature of the companion star. A main sequence companion star nearly filling its Roche lobe and of mass $> 0.13 M_{\odot}$ is associated with W whereas a brown dwarf under-filling its Roche lobe and of mass $< 0.03 M_{\odot}$ is associated with J. The X-ray luminosity of the non-thermal components from these MSPs can be estimated following the discussion given in §3.3. Taking an average spin-down power of the millisecond pulsars in 47 Tuc, $\dot{E} \sim 2 \times 10^{34} \text{ erg s}^{-1}$, $p = 2.3$, $\epsilon_B \sim 0.003$, $\epsilon_e \sim 0.5$, $\gamma_w \sim 10^6$, and $\Omega = 1$, we find a non-thermal X-ray luminosity in the band 0.1–10 keV of $4 \times 10^{29} \text{ erg s}^{-1}$ for an assumed $R_s \sim 10^{11} \text{ cm}$. If we choose $\epsilon_B \sim 0.1$, $\gamma_w \sim 2 \times 10^5$, a larger X-ray

luminosity $\sim 4 \times 10^{30} \text{ erg s}^{-1}$ results, which is closer to the observed values. This may suggest that ϵ_B in PWN of MSPs is indeed larger. The remaining deviation by a factor of 3 may suggest an underestimate of the spin down power of these millisecond pulsars by a factor of ~ 2 .

18.8.3 X-Ray Tails Associated with Pulsars

The X-ray emitting region with a characteristic frequency ($\nu_X = \frac{3\gamma^2 eB}{2m_e c}$) may exhibit a tail-like spatial structure provided that the pulsar velocity exceeds that of the termination shock front and the nebula magnetic field is sufficiently low. In this case, the distance traversed by the pulsar within the synchrotron cooling timescale can be taken as a lower limit of the elongation length. Specifically, the synchrotron cooling time in the X-ray band is $\tau_c = 6\pi m_e c / \gamma \sigma_T B^2 \sim 10^8 B_{mG}^{-3/2} (h\nu_X / \text{keV})^{-1/2} \text{ s}$ where B_{mG} is the magnetic field in the emission region in milli-gauss. Thus, the typical cooling time is $\sim 10^{11} \text{ s}$ for $B_{mG} = 0.01$, and the length of the X-ray elongated feature is about $l \sim v_p \tau_c \sim 10^{18} \text{ cm}$ for a pulsar moving at a velocity of 100 km s^{-1} with respect to the interstellar medium.

The X-ray images of some pulsar wind nebulae, indeed, reveal extensive X-ray tails. Seven cases are thought to be the consequence of a bow shock formed by the high velocity pulsar (e.g., Geminga, PSR B1823–13, B1757–24, B1957–20, J1747–2958, J1124–5916 and B1853+01). The two pulsars J1930+1852 and B0453–685 exhibit elongated structures and may also be bow shock structures. On the other hand, the Crab and Vela nebulae exhibit an outflow structure (X-ray jet). For more detail discussion of X-ray tails of pulsars (cf. [22, 23]).

18.9 Conclusion

In general, high energy radiations from pulsars can come from either polar gaps or outer gaps. However, from the light curve, optical emission and the energy dependent spectra of the Crab pulsar it is quite clear that they are emitted from the outer-magnetospheric regions rather than from regions near the surface. Slot gaps, which can extend to high altitudes, can also be possible alternative accelerators. However, the potential drop of the slot gap (e.g., [2]) is limited because it is connected at the polar cap. Therefore it is geometrically thin and the emission cone is quite small. It is not clear if such thin gap can provide enough power to explain the observed data in the Crab pulsar.

In order to explain the light curves and the phase-resolved spectrum of pulsars correctly, it is inevitably that three-dimensional models must be used. We have given a detailed model fitting for the phase-resolved data of the Crab pulsar. The general features of the data can be produced by the simple outer gap model. In particular, the detail optical polarization properties can be explained and the spectral break in

ultra-violet can also be obtained in the model (cf. [91]). The model also predicts that the polarization angle swing can only obtain if the viewing angle is larger than 90° . In model fitting it is important to note that the inner boundary of the outer gap cannot begin at the null charge surface otherwise the leading wing, trail wing and the off pulse can not be obtained.

We have suggested that the non-thermal non pulsed X-rays from the direction of pulsars may come from the pulsar wind nebulae. We estimate that the X-ray spin-down power and the non-thermal non pulsed X-ray luminosity should be related as $L_x \propto L^{p/2}sd$, where p is the index of the electron distribution and it is between 2 and 3 [22]. The pulsed non-thermal component of X-rays should follow $L_x \propto L^{1.15}sd$ [26]. Despite the orbital period, dipole magnetic field, rotation period and companion star for millisecond pulsars in the field and millisecond pulsar in the globular clusters are so similar, the structure of their surface may be very much different. Consequently most millisecond pulsars in globular cluster, e.g., 47 Tuc, are poor gamma-ray emitters and their X-rays are dominated by thermal X-rays [21, 81]. Since the shock radii of the pulsar wind nebulae for millisecond pulsars in the globular clusters are so large than the non-thermal emission from the nebulae will be excluded from observations. On the other hand it is interested in checking how much non-thermal X-rays from the pulsar wind nebulae of millisecond pulsars can contribute to the non-thermal X-ray emission from the entire cluster. Taking the characteristic conversion efficiency $\eta \sim 1\%(0.1\%)L_{sd}$ for the fast(slow) cooling process, the X-ray luminosity from the entire cluster contributed by the millisecond pulsars could be $10^{34}(\eta/10^{-2})(N/100) \text{ erg s}^{-1}$, where N is the number of millisecond in the globular cluster. It is interesting to notice that the tail length of the pulsar wind nebulae can be a nice data to estimate the local magnetic field [58, 59].

Although the general features of the Crab data can be produced by the simple outer gap model. However, a lot of fine details in data are still unable to be explained. Obviously, the detail electrodynamic structure of the accelerator in the outer magnetosphere must be studied more carefully. The successful missions of Chandra and XMM-Newton have already imposed great challenge for the existing theoretical models. After the launch of GLAST, we anticipate more challenging data will be observed. New theoretical models are anticipated to be produced to confront with all these new challenges.

References

1. M.A. Alpar, A.F. Cheng, M.A. Ruderman et al.: *Nature* **300**, 728 (1982)
2. J. Arons: Electron positron pairs in radio pulsars. In: *Positron-electron pairs in astrophysics; Proceedings of the Workshop, Greenbelt, MD, January 6–8, 1983*, ed by M.L. Burns, A.K. Harding, and R. Ramaty (New York: AIP 1983) pp. 163
3. J. Arons: In: *Neutron Stars and Pulsars*, eds. S. Shibata and M. Sato (Universal Academy Press, Tokyo, 1997)
4. J. Arons, E.T. Scharlemann: *ApJ* **231**, 854 (1979)
5. J. Arons, M. Tavani: *ApJ* **403**, 249 (1993)

6. W. Becker, B. Aschenbach: X-ray Observations of Neutron Stars and Pulsars: First Results from XMM-Newton. In: *Proceedings of the 270. WE-Heraeus Seminar on Neutron Stars, Pulsars, and Supernova Remnants. MPE Report 278*, ed by W. Becker, H. Lesch, and J. Trümper (Garching bei München: Max-Planck-Institut für extraterrestrische Physik 2002) pp. 64
7. W. Becker, J. Trümper: *A&A* **326**, 682 (1997)
8. W. Becker, J. Trümper: *A&A* **341**, 803 (1999)
9. V.S. Beskin, A.S. Gurevich, Ya.N. Istomin: *Physics of the Pulsar*, (Cambridge University Press, Cambridge 1992)
10. D. Bhattacharya: *JAA* **22**, 67 (2002)
11. G.F. Bignami, P.A. Caraveo: *Nature* **361**, 704 (1993)
12. G.R. Blumenthal, R.J. Gould: *Rev. Mod. Phys.* **42**, 237 (1970)
13. S. Bogdanov, J.E. Grindlay, M. van den Berg: *ApJ* **630**, 1029 (2005)
14. P.A. Caraveo, G.F. Bignami, A. de Luca et al.: *Science* **301**, 1345 (2003)
15. A. Cheng, M.A. Ruderman, P.G. Sutherland: *ApJ* **203**, 209 (1976)
16. K.S. Cheng, K.Y. Ding: *ApJ* **431**, 724 (1994)
17. K.S. Cheng, J. Gil, L. Zhang: *ApJ* **493**, L35 (1998)
18. K.S. Cheng, C. Ho, M.A. Ruderman: *ApJ* **300**, 500 (1986a)(CHRI)
19. K.S. Cheng, C. Ho, M.A. Ruderman: *ApJ* **300**, 522 (1986b)(CHRII)
20. K.S. Cheng, M. Ruderman, L. Zhang: *ApJ* **537**, 964 (2000)(CRZ)
21. K.S. Cheng, R.E. Taam: *ApJ* **598**, 1207 (2003)
22. K.S. Cheng, R.E. Taam, W. Wang: *ApJ* **617**, 480 (2004)
23. K.S. Cheng, R.E. Taam, W. Wang: *ApJ* **641**, 427 (2006)
24. K.S. Cheng, D.M. Wei: *ApJ* **448**, 281 (1995)
25. K.S. Cheng, J.L. Zhang: *ApJ* **463**, 271 (1996)
26. K.S. Cheng, L. Zhang: *ApJ* **515**, 337 (1999)
27. R.A. Chevalier: *ApJ* **539**, L45 (2000)
28. J. Chiang, R.W. Romani: *ApJ* **400**, 629 (1992)
29. J. Chiang, R.W. Romani: *ApJ* **436**, 754 (1994)
30. F.V. Coroniti: *ApJ* **349**, 538 (1990)
31. J.K. Daugherty, A.K. Harding: *ApJ* **252**, 337 (1982)
32. J.K. Daugherty, A.K. Harding: *ApJ* **458**, 278 (1996)
33. J. Dyks, B. Rudak: *ApJ* **598**, 1201 (2003)
34. J. Dyks, B. Rudak, A.K. Harding: *ApJ* **607**, 939 (2004)
35. T. Erber: *Rev. Mod. Phys.* **38**, 626 (1966)
36. J.M. Fierro, P.F. Michelson, P.L. Nolan et al.: *ApJ* **494**, 734 (1998)
37. D.K. Galloway, D. Chakrabarty, E.H. Morgan et al.: *ApJ* **576**, L137 (2002)
38. V.L. Ginzburg, S.I. Syrovatskii: *Ann. Rev. Astron. Astrophys.* **3**, 297 (1965)
39. T. Gold: *Nature* **218**, 731 (1968)
40. P. Goldreich, W.H. Julian: *ApJ* **157**, 869 (1969)
41. J.E. Grindlay: In: *363rd Heraeus Seminar: Neutron Stars and Pulsars Bad Honnef 14–19 May 2006* (2006)
42. J.E. Grindlay, F. Camilo, C.O. Heinke et al.: *ApJ* **581**, 470 (2002)
43. A.K. Harding: *ApJ* **245**, 267 (1981)
44. A.K. Harding: In: *363rd Heraeus Seminar: Neutron Stars and Pulsars Bad Honnef 14–19 May 2006* (2006)
45. A.K. Harding, A.G. Muslimov: *ApJ* **508**, 328 (1998)
46. A.K. Harding, V.V. Usov, A.G. Muslimov: *ApJ* **622**, 531 (2005)
47. A.K. Harding, B. Zhang: *ApJ* **548**, L37 (2001)
48. A. Hewish, S.J. Bell, J.D.H. Pilkington, P.F. Scott, R.A. Collins: *Nature* **217**, 709 (1968)
49. K. Hirotani: *Ap&SS* **297**, 81 (2005)
50. K. Hirotani: *ApJ* **652**, 1475 (2006)
51. K. Hirotani, A.K. Harding, S. Shibata: *ApJ* **591**, 334 (2003)
52. K. Hirotani, S. Shibata: *MNRAS* **308**, 54 (1999a)
53. K. Hirotani, S. Shibata: *MNRAS* **308**, 67 (1999b)
54. K. Hirotani, S. Shibata: *PASJ* **51**, 683 (1999c)

55. K. Hirotani, S. Shibata: *MNRAS* **325**, 1228 (2001)
56. C. Ho: *ApJ* **342**, 396 (1989)
57. N.J. Holloway: *Nature Physical Science* **246**, 6 (1973)
58. C. Y. Hui, W. Becker : *A&A*, 2006a, 448, 13
59. C. Y. Hui, W. Becker : *A&A*, 2006b, 457, 33
60. J.J. Jia, A.P.S. Tang, J. Takata, H.K. Chang, K.S. Cheng: 2007, *AdSpR*, 40, 1425
61. P.B. Jones: *MNRAS* **192**, 847 (1980)
62. G. Kanbach, A. Slowikowska, S. Kellner, H. Steinle: New optical polarization measurements of the Crab pulsar. In: *Astrophysical Sources of High Energy Particles and Radiation. AIP Conference Proceedings*, vol. 801, pp. 306 (2005)
63. C.F. Kennel, F.V. Coroniti: *ApJ* **283**, 710 (1984)
64. L. Kuiper, W. Hermsen, G. Cusumano et al.: *A&A* **378**, 918 (2001)
65. M.I. Large, A.F. Vaughan, B.Y. Mills: *Nature* **220**, 340 (1968)
66. C.B. Markwardt, E. Smith, J.H. Swank: *IAU Circ. No. 8080* (2003)
67. C. Markwardt, J.H. Swank, T.E. Strohmayer et al.: *ApJ* **575**, L21 (2002)
68. E. Massaro, G. Cusumano, M. Litterio et al.: *A&A* **361**, 695 (2000)
69. F.C. Michel: *Theory of Neutron Star Magnetospheres*, (University of Chicago Press, Chicago, 1991)
70. A.G. Muslimov, A.K. Harding: *ApJ* **485**, 735 (1997)
71. A.G. Muslimov, A.I. Tsygan: *MNRAS* **255**, 61 (1992)
72. F. Pacini: *Nature* **219**, 145 (1968)
73. E.S. Phinney, S.R. Kulkarni: *ARA&A* **32**, 591 (1994)
74. A. Possenti, R. Cerutti, M. Colpi et al.: *ApJ* **387**, 993 (2002)
75. V. Radhakrishnan, F. Srinivasan: *Current Science* **51**, 1096 (1982)
76. M.J. Rees, J.E. Gunn: *MNRAS* **167**, 1 (1974)
77. D.W. Richards, J.M. Comella: *Nature* **222**, 551 (1969)
78. R.W. Romani: *ApJ* **470**, 469 (1996)
79. R.W. Romani, I.A. Yadigaroglu: *ApJ* **438**, 314 (1995)
80. M. Ruderman: Evolution and radiation in pulsar polar CAP models. In: *Pulsars: 13 years of research on neutron stars; Proceedings of the IAU Sym. 95, Bonn, West Germany, August 26–29, 1980*, ed by W. Sieber, R. Wielebinski (Dordrecht: Reidel, 1981) pp. 87
81. M. Ruderman, K.S. Cheng: *ApJ* **335**, 306 (1988)
82. M. Ruderman, J. Shaham, M. Tavani: *ApJ* **336**, 507 (1989)
83. M. Ruderman, P.G. Sutherland: *ApJ* **196**, 51 (1975)
84. Y. Saito: Title. PhD Thesis, Univ. Tokyo (1998)
85. F.D. Seward, Z.R. Wang: *ApJ* **332**, 199 (1988)
86. D.H. Staelin, E.C. Reifstein: *Science* **162**, 1481 (1968)
87. B.W. Stappers, B.M. Gaensler, V.M. Kaspi et al.: *Science* **299**, 1372 (2003)
88. L. Stella, S. Campana, M. Colpi et al.: *ApJ* **423**, L47 (1994)
89. P.A. Sturrock: *ApJ* **164**, 529 (1971)
90. J. Takata, S. Shibata, K. Hirotani: *MNRAS* **354**, 1120 (2004)
91. J. Takata, H.K.Chang, K.S. Cheng: *ApJ* **656**, 1044 (2007)
92. A.P.S. Tang: *The Physics of Neutron Stars*. PhD Thesis, Univ. Hong Kong (2007)
93. M. Tavani, J. Arons: *ApJ* **477**, 439 (1997)
94. D.J. Thompson: In: *363rd Heraeus Seminar: Neutron Stars and Pulsars Bad Honnef 14–19 May 2006* (2006)
95. D.J. Thompson , M. Bailes, D.L. Bertsch et al.: *ApJ* **465**, 385 (1996)
96. V.V. Usov: *ApJ* **427**, 394 (1994)
97. E.P. van den Heuvel, J.A. van Paradijs, R.E. Taam: *Nature* **322**, 153 (1986)
98. F.Y.-H. Wang, M. Ruderman, J.P. Halpern, T. Zhu: *ApJ* **498**, 373 (1998)
99. M.C. Weisskopf, J.J. Hester, A.F. Tennant et al.: *ApJ* **536**, L81 (2000)
100. R. Wijnands, M. van der Klis: *Nature* **394**, 344 (1998)
101. I.-A. Yadigaroglu, R.W. Romani: *ApJ* **449**, 211 (1995)
102. V.E. Zavlin, G.G. Pavlov, D. Sanwal et al.: *ApJ* **569**, 894 (2002)
103. B. Zhang, A.K. Harding: *ApJ* **532**, 1150 (2000)
104. L. Zhang, K.S. Cheng: *ApJ* **487**, 370 (1997)
105. L. Zhang, K.S. Cheng, Z.J. Jiang, P. Leung: *ApJ* **604**, 317 (2004)